© von Karman Institute for Fluid Dynamics
Waterloosteenweg 72 – 1640 Sint-Genesisu-Rode

Dear reader,

The electronic document attached is protected by copyright laws.

This article may be used for research, teaching and private study purposes. Any substantial or systematic reproduction, redistribution, reselling, loan, sub-licensing, systematic supply, or distribution in any form to anyone is expressly forbidden.

Please do not distribute the document to third parties outside your workgroup as under current copyright law it is only intended for your personal scientific use. If you do not comply with the above conditions of use, you may be held liable for copyright infringement.

VON KARMAN INSTITUTE FOR FLUID DYNAMICS

LECTURE SERIES 1984-03

DIGITAL IMAGE PROCESSING IN FLUID DYNAMICS

MARCH 5-9, 1984

LASER SPECKLE VELOCIMETRY IN FLUID DYNAMICS APPLICATIONS

R. MEYNART - VKI & U.LIBRE DE BRUXELLES, BELGIUM
SENIOR RESEARCH ASSISTANT FNRS

L. M. LOURENÇO - VKI

ABSTRACT

A novel flow visualization and velocity measurement technique is described. It permits the simultaneous visualization of instantaneous two dimensional streamline patterns in unsteady flows, and the quantification of the velocity field.

The technique involves seeding the flow with small particles and lighting the plane of interest with a sheet of pulsed laser light to obtain multiple exposure photograph of the particles as they travel with the flow.

The multiple particle images provide the streamlines in the limit of short duration between laser pulses. The local velocity information is retrieved using an optical method. The photographic negative is analyzed by passing a probe laser beam through each point of interest and allowing the diffraction produced by the multiple particle images to generate fringes in the Fourier plane of a lens. These fringes have an orientation which is perpendicular to the direction of the local velocity vector and a spacing which is inversely proportional to its magnitude.

The parameters involved in obtaining multiple exposure photograph are discussed and a relation is established between these parameters. The overall accuracy of the measurement technique is also discussed. Finally, examples of application of the technique in various flows are presented.

1. INTRODUCTION

Knowledge of flow field streamline patterns as well as velocity and vorticity is crucial to the understanding of fluid flow phenomena. While hot wire anemometry and laser doppler velocimetry (LDV) are the most widely used techniques for velocity measurements, their usefulness is limited to stationary flow applications where conclusions can be reached from velocity information acquired sequentially one point at a time. Of these, the LDV, due to its non-invasive characteristics and ability to resolve reverse flows, is the most useful tool for measurement of average velocities in stationary flows. These systems, however, cannot provide data to study the time evolution of flows that evolve stochastically in both space and time.

To fill this gap many investigations have relied on flow visualization techniques using dye injection or hydrogen bubbles in the case of liquid flows, or smoke injection and smoke wire techniques in the case of air flows. This does provide streakline patterns, but despite the fact that valuable information can be derived from the visualizations, the problem of obtaining an instantaneous velocity map remains. Moreover data obtained from streaklines in unsteady flows must be interpreted with care (Ref. 1).

Other more sophisticated techniques like streak photography or double exposure techniques of a seeded flow are often used but with limited success (Refs.2,3). The reduction of the large amount of information contained in the photograph is far from easy, and the velocity measurements have an associated error which becomes important when the length of the streak, in streak photography, or the spacing between successive tracer images, in double exposure techniques, is small. Another problem is that these methods fail to provide accurate results when the mean distance between tracers is of the same order of magnitude as the distance a tracer particle travels during

the exposure time, in streak photography, or the time between exposures, in double exposure techniques. As a consequence the tracer concentration is usually kept small resulting in velocity measurements with poor spatial density. Recently, rather involved interpolating methods have been designed (Ref. 3) to increase the spatial resolution of the techniques, but their validity is questionable, considering that in most interesting flows, e.g. separated, turbulent, the distance between data points is larger than the flow scales.

Here we describe a novel measurement technique (Refs. 4-9) that provides the ability to instantaneously measure velocities in a two dimensional field while retaining the non-invasive characteristics of the LDV. It is a multiple exposure technique permitting the visualization of two dimensional streamline patterns, as well as quantification of the flow field.

The major difference from conventional multiple exposure methods lies in the processing methods for the retrieval of local velocity information. In the present technique an optical processing method usually applied to analyze speckle photographs in solid mechanics is employed. Because of the similarity with conventional speckle methods the velocity measurement technique is referred to as "Speckle Velocimetry".

2. APPLICATION OF LASER SPECKLE TO FLUID FLOW VELOCITY MEASUREMENTS

2.1 Principles

Similarly to LDV, the speckle technique involves seeding the flow with small tracer particles. A sheet of coherent light is used to provide a "surface" within the fluid. A laser is used as the light source. A pulsed laser such as a Ruby or NdYag laser, or a CW laser with a shutter device can be used, to pulse the illumination sheet for the multiple exposure. The laser sheet is formed for example by focusing the laser beam first with a long focal length, to obtain minimum thickness, and then diverging the beam in one dimension with a cylindrical lens (Fig. 1).

The scattering by the seeding particles in the illuminated plane provides a moving pattern. This pattern consists of resolved diffraction limited images of the particles when the seeding concentration is low. When this concentration increases, the images overlap and interfere to produce a random pattern called speckle. As the seeding particles move the corresponding pattern moves accordingly and consequently a double exposed photograph records two identical but relatively shifted patterns. The image formed by isolated Airy disks, in the case of low seeding concentrations, or speckle grains for high seeding concentrations, is a complicated random pattern whose displacement can hardly be measured by visual or computer-aided inspection. However, it is important to realize that the multiple exposure photograph results in a periodic random image from which the periodicity information can be retrieved using Fourier analysis.

Two dimensional Fourier transformation of the image can be performed by optical processing of the photographic negative. This process produces, as explained in the following, a straight fringe pattern whose orientation and magnitude are related to the direction and magnitude of the displacement.

Consider the function $D(\vec{r})$ describing the light intensity in the image plane of a photographic camera, where $\vec{r}(x,y)$ are the plane coordinates. Considering that there is an in-the-plane displacement dy of the scatterers, the image will be translated by Mdy, where M is the magnification of the camera lens, and the intensity function becomes $D(x,y+Mdy)$. The function representing both intensity distributions is

$$D(x,y) + D(x,y+Mdy) = D(x,y) \otimes \left[\delta(x,y)+\delta(x,y+Mdy)\right] \qquad (1)$$

where $\delta(x,y)$ is the Dirac delta function centered on $\underline{r}(x,y)$, and considering that a translation can be represented as a convolution with a delta function. The total intensity is recorded on photographic plate. After development the transmittance, τ, of the negative is given by

$$\tau(\vec{r}) = a+bD(x,y) \otimes \left[\delta(x,y)+\delta(x,y+Mdy)\right] \qquad (2)$$

where a and b are characteristic constants of the photographic emulsion. Local analysis of the film negative with a probe laser beam (Fig. 2) produces in the focal plane of a lens a two dimensional Fourier transform of the transmittance distribution, $\tilde{\tau}$, as follows,

$$\tilde{\tau}(u,v) = a\delta(u,v) + b\tilde{D}(u,v)\left[1+\exp(i2\pi vMdy/\lambda_a)\right] \qquad (3)$$

where $\tilde{\tau}$ represents the Fourier transform of τ, u and v are the angular coordinates of a point in the Fourier plane of the lens, and λ_a is the wavelength of the interrogating laser light beam.

The first term, $a\delta(uv,)$ on the r.h.s. of equation (3) represents the image of a point source, i.e. the interrogating beam, when diffraction effects are neglected. This image is seen as a small bright spot in the center of the Fourier plane (Fig. 2). The second term is composed by a fine speckle structure, $\tilde{D}$ (diffraction halo) modulated by $\left[1+\exp(i2\pi vMdy/\lambda_a)\right]$

The intensity distribution for the second term is obtained by multiplication with its complex conjugate, resulting in

$$|\tilde{D}(u,v)|^2 \left[4\cos^2(\pi v M dy/\lambda_a)\right] \tag{4}$$

The diffuse background, $|\tilde{D}|^2$, (called "diffraction halo") is modulated by a set of Young's fringes whose spacing is given by

$$d_F = \frac{\lambda_a f_L}{M dy} \tag{5}$$

where f_L is the focal length of the converging lens. Knowing M, f_L, λ_a and measuring d_F the displacement dy is easily found from equation (5), with the direction of motion perpendicular to the orientation of the fringes.

By scanning the double exposed photograph one can resolve the two components of the velocity vector at every point of the field. This is a unique feature of the laser speckle technique.

The principle of this analysis technique has been widely used in solid mechanics to measure the displacement field of scattering surfaces illuminated with a coherent light beam. In this case, the diffusive object behaves like a surface composed of a very large number of spatially incoherent point sources. The light waves emitted by the sources interfere and a random speckle pattern is formed in space. This speckle can be recorded on a photographic plate and constitutes the random microstructure whose displacement is measured by optical Fourier transformation.

Speckle techniques are used in many useful applications, e.g. the study of object displacement and rotation, surface roughness and astronomy. The development of speckle methods constitute in itself a new chapter in optics.

2.2 Limitations of the conventional speckle technique

The main restriction in the use of speckle techniques are related to the formation of the scattering sheet and to the measurement of flows where the fluid motion has important components in the direction perpendicular to the illumination plane (out-of-plane movement).

The production of a true speckle pattern by scattering from a seeded flow necessitates high particle concentration. In such a case, multiple scattering effects can spread the thin light sheet very rapidly. Furthermore, the absence of interaction between the flow and the large number of traces is questionable.

As shown in the previous paragraph the technique relies on the recording of two identical speckle patterns that have been laterally shifted. Slight out-of-plane motion of the scatterers, between the two exposures, results in two speckle patterns that are not entirely similar and therefore are less correlated. As a consequence the fringe contrast will decrease or in the extreme case will be lost.

This poses severe restrictions in the use of "pure" speckle techniques for the measurement of velocities in turbulent fields. To cope with these problems, instead of conventional speckle, where a random interference pattern is stored, the individual particle images can be imaged and resolved (Refs. 5-7). It is found that this procedure is less sensitive to out-of-plane motion. In this case the tolerance to the out-of-plane motion is roughly equivalent to the width of the illumination sheet.

In the present technique the methods developed for the analysis of "pure" speckle remain valid as well as the relations between the fringe pattern and the local particle displacement.

2.3 Fringe sharpness versus number of exposures

The degree of accuracy with which one can determine the fringe spacing depends greatly on the contrast and sharpness of Young's fringes.

If the number of exposures is increased (>2), and the particles are displaced by the same amount after each exposure, the sharpness of the interference fringes can be improved. This is demonstrated by the following.

For a multiple exposure the intensity function becomes :

$$D(x,y) \otimes \sum_{n=0}^{N-1} \delta(x,y+nMdy) \qquad (6)$$

resulting in an amplitude distribution of the transmittance of the negative in the Fourier plane as follows,

$$\tau(\underline{x}) = a+bD(x,y) \otimes \sum_{n=0}^{N-1} \delta(x,y+nMdy) \qquad (7)$$

The intensity function is therefore

$$|\tilde{D}(u,v)|^2 \left[N+2 \sum_{n=1}^{N-1} n \cos\left((N-n)2\pi Mdy/\lambda_a\right) \right] \qquad (8)$$

For a number of exposures, N, equal to 2, a relation similar to equation (4) is obtained as expected.

Figure 3 displays the fringe width for multiple exposures, normalized with the corresponding width for double exposure, versus the number of exposures. It is clearly seen

that an optimum fringe width can be obtained with a limited number of exposures. Another illustration of this effect is shown in figures 4a-d which display a two dimensional Fourier transform of respectively 2, 4, 6 and 8 equidistant and aligned point sources in a dark background.

The sharpening of the fringes using a multiple exposure recording technique is of great advantage because it allows a very easy visual and qualitative "measurement" of the direction and spacing of the Young's fringes. It also increases the signal to noise ratio of the intensity pattern recorded by the analysis setup. Note that the improvement in the SNR is also the result of the artificial increase in particle concentration due to the multiple exposure.

2.4 Velocity measurement by spatial filtering

Processing the photograph with a conventional spatial filter (Fig. 5) provides directly a velocity map of the two dimensional flow pattern. This method is fast and convenient. The transmittance of the photograph is given by

$$\tau(\vec{r}) = a+b\left[D(\vec{r}) \otimes \sum_{k=0}^{N-1} \delta(\vec{r}+kM\vec{d})\right] \qquad (9)$$

where $\vec{r}$ is the position vector and $\vec{d}$ the displacement.

In the Fourier plane (FP in Fig. 5), the amplitude is expressed in the form :

$$U(\vec{r}_f) = TF\left[T(\vec{r})\right] P(\vec{r}_f) \qquad (10)$$

where $\vec{r}_f$ is the position vector in the Fourier plane, TF means a two dimensional Fourier transfrom and $P(\vec{r}_f)$ is the transmittance of the filter.

If the filter is a circular hole (with radius a), whose center is located at $\vec{r}_0$, corresponding to a spatial frequency $\vec{f}_0 = \vec{r}_0/\lambda_f$, the intensity in the image plane (I in Fig. 5) may be expressed by

$$I(\vec{r}_p) = C \left| \tau(-\vec{r}_p) \otimes \left[\exp(-2\pi j \vec{r}_p \vec{f}_0) \frac{J_1(2\pi r_p a/\lambda_f)}{(2\pi r_p a/\lambda_f)} \right] \right|^2 \qquad (11)$$

where $\vec{r}_p$ is the position vector in the image plane, C is a constant, λ is the wavelength and f is the focal length of the transform lenses.

The convolution in equation (11) will be extremum in the regions where the projection Md_p of the displacement on the direction defined by the filtering hole is a multiple of the period of the oscillatory term $\exp(-2\pi j \vec{r}_p \vec{f}_0)$. The projected displacement d_p obeys the relation $Md_p = n\lambda/\theta$, where n is an integer and θ the angle shown in figure 5. Thus isovelocity contours are drawn by the spatial filter as illustrated in §6.1. The interferences between independent particles contained in the area defined by the factor $J_1(2\pi r_p a/\lambda f)/(2\pi r_p a/\lambda f)$ in equation (11) produce the speckle present in the filtered image (see § 6.1). It must be pointed out that the quality of the isovelocity fringes is essentially a result of the multiple exposure technique. The multiple beam interference causes the same sharpening and increase in brightness of the isovelocity fringes as in a Fabry-Pérot interferometer.

3. A GUIDELINE FOR THE CHOICE OF THE PARAMETERS INVOLVED IN A MEASUREMENT USING MULTIPLE EXPOSURE PHOTOGRAPHY

The different parameters playing a role in measurements using multiple exposure photography can be classified as follows :

1. Exposure parameters : time between exposures, exposure time and number of exposures.
2. Film parameters : film sensitivity, resolution and grain.
3. Tracer : type, concentration and dimensions.

These parameters are interrelated and depend upon the flow field of interest, namely the velocity range, the area in which the two dimensional map of velocities is to be obtained and the required spatial resolution of the measurement.

3.1 Exposure parameters

The exposure parameters are chosen in accordance with the maximum expected velocity in the field and the required spatial resolution. The spatial resolution is dictated by the scales involved in the fluid motion and should be better than the smallest scale.

1. The time between exposures, T, is determined by the maximum permissible displacement of a particle such that a correlation is possible when locally analysing the film negative with a laser beam.

A necessary condition to obtain Young's fringes when locally illuminating the film with a probe laser beam requires that the distance between the adjacent particle images is less than a fraction of the analysing beam diameter.

A practical value for this maximum displacement is about D/2 (the beam radius). Putting in analytical terms :

$$Mv_{max}T \cong 0.5D \tag{12}$$

$$T \simeq \frac{0.5D}{Mv_{max}} = \frac{1}{f} \tag{13}$$

where M is the magnification factor, D and λ_a are respectively the interrogating beam diameter and laser light wavelength, v_{max} the maximum expected velocity in the field, and f the frequency corresponding to the inverse of the period T.

As has been pointed out in section 2, multiple exposures increase the sharpness of Young's fringes. In this case the time interval between two consecutive pulses is unchanged and equation (13) remains valid, but in some applications where the SNR of the fringes is very poor, it may be interesting to decrease T and multiple expose the photograph to improve the SNR. However, this procedure has the drawback of reducing the velocity dynamic range as will be shown in the next section.

2. The exposure time, t, becomes a free parameter only when a CW laser source is used together with a shutter. In principle this parameter should be kept as small as possible. However, as shown below, (§ 3.3), the maximum velocity that can be measured using a CW laser depends strongly on this parameter and it is directly proportional to it. In most of the commercially available pulsed laser sources, the pulse time is very short and of the order of 10-30 ns.

In previous experiments, using a CW laser source (Ref. 6) pulse durations as large as one twentieth of the time between pulses were used without significant problems. This leads to :

$$t = \frac{T}{K} = \frac{}{Mv_{max}K} \qquad (14)$$

where K is a constant of about 20.

The value of the constant K can be justified by the following argument. The image of a tracer particle is well recorded when its displacement during the recording time is less than the diameter of its image. In practical conditions (F # 5, M = 1, λ_r = .7 µm) the diameter d_i of the image of a point source is about 20-30 micron.

Considering a maximum displacement of about 200 micron and assuming that the maximum displacement during the exposure time is 10 micron we obtain :

$$K = \frac{T}{t} \simeq \frac{200}{10} = 20 \qquad (15)$$

The previous parameters together with the particle dimensions are used to determine the velocity dynamic range of the technique.

To produce an interference pattern (Young's fringes) the particle images have to be at least one particle image apart. This dictates the minimum velocity which can be resolved in the flow field,

$$v_{min} = \frac{d_i}{T} = \frac{2d_i Mv_{max}}{D} \qquad (16)$$

where d_i is the dimension of the particle image. This image is the result of the convolution of three optical patterns, whose sizes are given as follows, neglecting aberrations, grain noise and non linear effects :

$$\left[\begin{array}{l} dM \\ 2.44\lambda_r(1+M)F\# \\ Mvt \end{array} \right] \quad (17)$$

The first one being the particle diameter, the second one the edge spread caused by the limited response of the recording optics, and a third one accounting for the particle displacement during the exposure time, with F# the recording optics aperture F number.

The difference $v_{max}-v_{min}$ is the velocity dynamic range, and we obtain :

$$v_{max}-v_{min} = v_{max}\left[1-(2d_iM/D)\right]$$

As one would expect the smaller the particle size in the image plane, d_i, the larger the dynamic range.

3.2 Choice of the film

Having established the exposure parameters, one has to choose the characteristics of the recording optics (camera) and the film according to the available laser power.

The amount of power scattered by a tracer particle that is viewed by the camera is a function not only of the incident laser power but also of the particle and viewing optics characteristics.

The power density I_s at the center of the image of a tracer particle can be computed as follows

$$I_s = I \cdot Q_{scat} \cdot S_p \quad (19)$$

where S_p is the particle cross section and Q_{scat} is a parameter accounting for the scattering efficiency of the particles and

also depending on the viewing optics (Ref. 10). This parameter is a constant for given particles, given magnification and lens aperture. If I is the laser power at the center of the light sheet of width w and height h (width and height measured at the $1/e^2$ intensity points of the Gaussian shaped sheet), we have

$$I = \frac{2P_L}{\pi wh} = \frac{2P_L}{\pi S_T} \tag{20}$$

where P_L is the continuous laser power and S_T is defined as the cross section area of the laser sheet.

In order to successfully expose a particular photographic emulsion the energy scattered by the tracer has to be at least or larger than the film sensitivity, S, for a density of about 1 :

$$I_S \cdot t \geqslant S \tag{21}$$

Considering that one uses a continuous laser source we obtain :

$$\frac{P_L \cdot Q_{scat} \cdot D \cdot S_p}{\pi \cdot K \cdot M \cdot v_{max} \cdot S_T} \geqslant S \tag{22}$$

For a pulsed laser source the pulse duration is fixed, and it is more convenient to use directly the energy delivered (E_L) :

$$S_p \frac{2E_L}{\pi S_T} \cdot Q_{scat} \geqslant S \tag{23}$$

In the case a CW laser is used equation (22) shows that there is a relation between the required laser power and the flow velocity. One obtains the maximum measurable velocity for a particular laser power, flow geometry S_T, spatial resolution D, recording optics magnification M, and film sensitivity S,

$$v_{max} = \frac{P_L \cdot Q_{scat} \cdot D \cdot S_p}{K \cdot M \cdot S \cdot S_T \cdot \pi} \qquad (24)$$

Note that Q_{scat} depends on M.

In applications where a CW laser is used it may be possible to extend the maximum measurable velocity by increasing the film sensitivity. However, the choice of a faster film is limited by its grain size, which must be much smaller than the diameter of the tracer image, d_i. If this is not the case, then when illuminating the negative to produce Young's fringes, the film unexposed grains can introduce amplitude and/or phase changes into the wavefront of the analyzing laser beam and thus create additional noise. This noise has generally a frequency content which is in the same range as Young's fringes. Therefore its elimination is difficult either from optical or digital filtering. Film grain cannot be totally eliminated and it will always be present in different degrees especially in applications where fast film is used, to cope with low power density of the illumination sheet.

A method of solution has been proposed (Refs. 12,13) by which this source of noise is almost totally eliminated. It consists of producing a positive copy by contact printing on a very high resolution, fine grain film (Kodak Ortho, Agfa-Gevaert 8E56 holographic plates, etc). This film is now analyzed in the same fashion using the laser probe beam. Figures 6 a and b show respectively the interference fringes generated when analyzing the film negative and corresponding positive. As one can see there is a remarkable decrease in the noise level. Another advantage of using this procedure is that the central zero order spot due to the illumination beam is also eliminated.

Another very important drawback of the use of highly sensitive films is the poor resolution of these films. This poor resolution, related to the large grain, leads to important

inaccuracies in the velocity measures. In order to keep these inaccuracies beyond a tolerable level, films with a grain appreciably smaller than the image diameter must be chosen.

Films with a resolution of about 300 lines/mm and sensitivity ranging from 25 to 100 ASA (Agfa Ortho 25, Kodak Technical Pan 2415) are suitable for use when good precision is necessary. Note that a more sensitive film can still show a fairly good resolution (Kodak Royal-X Pan, 1250 ASA, resolution ≃ 100 lines/mm). The use of such films can be recommended when only a low precision estimate of the velocity field is requested.

3.3 Tracers

Tracers usually employed in experiments involving LDV are, generally speaking, appropriate for "speckle velocimetry". Along them the most commonly used are oil fogs and smoke in air flows, and natural seeding, titanium dioxide, latex particles and hydrogen bubbles in liquid flows.

The choice of the tracer dimensions depends on the flow field to be investigated and on the spatial resolution and dynamic range required in the measurement.

It is found that good results are obtained when varying their concentration within reasonable ranges. For optimal results one should consider that several particle images should be present in the area covered by the analyzing beam diameter.

The particle concentration should be less than a limiting value, above which a true speckle pattern will be formed due to the interference of the light scattered by the individual particles. If c is the particle concentration and w the width of the laser sheet, the mean apparent distance between particles in the illuminated plane must be larger than the diameter of the images, or :

$$\sqrt{\frac{1}{wc}} \gg d_i \qquad (25)$$

Considering typical values for d_i = 20-30 μm and w = 500 μm, we obtain $c \ll 5.10^{12}\ m^{-3}$. On the other hand, the illumination sheet has to keep its shape during its travel in the seeded fluid. The length ℓ of this path must be somewhat smaller than the mean free path (λ) in the medium.

$$\ell \lesssim \lambda = \frac{1}{C\ S_p} \qquad (26)$$

For 1 = .3 m and monodispersed particles with a diameter of 5 μm we have $S_p \cong \pi d^2/2$ (Ref. 9) and $c < 8\ 10^{10}\ m^{-3}$.

The condition for independent scattering has been established for uniformly sized particles (Ref. 9), and states that the center-to-center distance between particles must be larger than 3 radii. This corresponds to a rather high volume fraction of about 15%. Therefore this can be met using reasonable operating conditions.

A practical value of the concentration can be found by considering a light sheet of width w scanned with a beam whose diameter is D. Assuming that we have 10 particles in this volume, we obtain

$$c = \frac{10}{w\pi\ \frac{D^2}{4}} \qquad (27)$$

which corresponds to a concentration of about $10^{11} m^{-3}$ for w = D = 500 μm.

3.4 Conclusion

For a particular testing condition a working diagram can be constructed to include the parameters previously discussed. This is shown in figure 7. It is a three lobe diagram. One can determine, in lobe 1, for a given flow, for laser power (if a CW laser is used) and for required spatial resolution, the maximum measurable velocity from equation 22. Lobe 2 gives the required frequency of exposures depending on the desired number of exposures per measurement. Finally, the dynamic range can be found in lobe 3 for various ratios $\frac{d_i}{D}$. It can be seen that the dynamic range can be increased with decreasing $\frac{d_i}{D}$, but it should be kept in mind that for best results, d_i has to be much larger than the film grain size.

4. DIGITAL PROCESSING

The VKI digital image analtsys system is presented in figure 8. The fringe images are acquired and digitized via a black and white camera, RCA TC-1005/U01X, into a Digital Image Processor. The camera provides a TV and a synchronization signal. The video signal is memorized on two Matrox video boards, URGB-256/4es, the memories being continuously updated. These boards have a 256×256 pixels resolution and each 4 bit per pixel. The combination of the two cards doubles the number of bit per dot (8) allowing up to 256 grey or false color scales. The URGB-256 cards have built-in a high speed 8 bit video D/A con verter and a 8 bit grey scale/color encoders. These encoders supply a video black/white or color output which is displayed on a video monitor (MTX 3602 URBG). A separate frame grabber, Matrox UFG-01/8 is available allowing the URGB-256 image memories to store TV pictures. This frame grabber has a definition of 8 bit per pixel. The system is computer (PDP 11/34) controlled through a unibus interface. Transfer of the Matrox URGB-256 memory to the computer magnetic or floppy disks is also possible. The fringe processing system is shown in figure 9. The camera C is focused on the plane F where the Fourier transform of the illuminated region (0.5 mm diam) is located. The picture can be digitized in 256×256 pixels (with 8 bits resolution) which are transferred into the computer. In this case, the fringes fill only the central portion of the picture (128×128 points) because a high sampling frequency is not necessary to analyze these fringes. In the following sections we describe two complementary methods for fringe analysis and discuss their implications (Refs 6, 7).

4.1 Method 1 : One dimensional averaging

Interactive processing of the fringes can be performed easily by a simple method currently used in solid mechanics. The principle is to obtain a periodic signal by averaging over the lines (or the columns) of the picture. However, it is necessary to measure independently the angle of the fringes, which is performed by superimposing a computer-generated line on the

the digitized picture and adjusting its direction until it is parallel to the fringes. Being I(m,n) the digitized intensity, α the angle of the fringes along the n axis and if (63,63) are the coordinates of the center of the picture, then the frequency of

$$f(m) = \sum_{n=0}^{127} I\left[m+(n-63)\tan\alpha, n\right] \qquad 0 \leqslant m \leqslant 127 \qquad (28)$$

is proportional to the velocity component along the m axis. Note that this procedure eliminates the need for mechanical rotation of the fringes. Further Fourier processing of f(m) yields the value of its periodicity (Fig. 10a). However, it can be shown (see eq. 4, § 2.1) that f(m) is the product of an envelope waveform which results from the diffraction halo. The Fourier transform of f(m) is the convolution of a Dirac distribution with the transform of the envelope which can be a broad function with important sidelobes. To minimize the linewidth, a constant amplitude periodic function must be recovered from f(m). In solid mechanics, the envelope can be evaluated by integrating the fringe intensity along a direction perpendicular to the fringes. Because of the difficulty to measure this envelope in fluid mechanics applications (see Fig. 10c), the minimization procedure is performed by computing the logarithm of f(m) (Figi 10a). This logarithmic transformation is based on the cepstrum technique used in acoustics and transforms the product constituting f(m) into the sum of a nearly constant amplitude function and a slowly varying waveform (see Fig. 10a). As a result, the power spectrum of logf(m) will show a narrow peak at the fringe frequency. However, this operation decreases the SNR and the Fourier transform shows noisy components (Fig; 10). The logarithm computation introduces an important noise level in the far wings of f(m) where it is low-valued. In addition, the Fourier transform of the rectangular window shows important sidelobes. Then, if the frequency of the fringes is not too low it is more convenient to decrease the noise and the importance of the sidelobes than to minimize the linewidth. This can be achieved by multiplying

logf(m) by a window function having a low value near the extremities of the interval and showing very weak sidelobes. Figure 10b illustrates the results obtained with a Hanning window.

The main advantage of the one dimensional averaging technique is rapidity. The computation is completed in a few seconds with a minicomputer PDP 11/34 used in a time-sharing environment. The second advantage is the possibility to obtain an evaluation of the frequency in the case of very low fringe densities by spectral analysis of logf(m). Note, however, that this technique does not always clearly yield identifiable peaks. The results are more reliable for convection flow measurements (Ref. 6); this is probably due to the use of multiple exposures when the flow is sufficiently slow so that it can be illuminated by more than two pulses from a chopped CW laser. Then Young's fringes are thinner and brigher; as a result, the SNR increases and the spectra of logf(m) have higher quality.

4.2 Method 2 : Averaged autocorrelation technique

The inconvenience of the one dimensional averaging method is the need for an external adjustment of the angle of the fringes. This problem can be bypassed by computing successively the velocity components along independent directions. Because each line of the picture can be considered as a noisy periodic signal with a variable phase, the automatic determination of a velocity component can be performed only by averaging over a quantity independent of the phase. The autocorrelation of each line or its Fourier transform the power spectrum satisfies this requirement.

The m velocity component can be computed from :

$$g(u) = \sum_{n=0}^{127} \left[\frac{\sum_{m} \left(I(m,n) I(m+u,n) \right)}{\sum_{m} \left(I(m,n) \right)^2} \right] \qquad -127 \leqslant u \leqslant 127 \qquad (29)$$

The individual autocorrelations in g(u) are normalized to give an an equivalent weight to each line. Note that the lines where the periodic signal is too weak are discarded from the sum. The discrimination is based on the mean intensity of the line. The averaged autocorrelation g(u) exhibits an important peak around u=0 which is mainly due to the speckle present in the fringes (Fig. 10) The height of this peak can be decreased by constructing

$$g'(u) = \frac{g(u)}{(1+\exp(-u^2/p^2))} \qquad (30)$$

where p is an adjustable parameter. As a result, the resolution of the peaks of |FFT g'(u)| is improved (Fig. 11).

By computing the averaged autocorrelation of the columns of I(m,n), the n component can be computed. It must be noted that more than two components are generally necessary for measuring the two dimensional velocity with accuracy. For example, in the present case, the y component is usually weak and the corresponding averaged autocorrelation exhibits only few peaks. The y component can, however, be extracted by measuring the components along two axes oriented at +45° and -45° with respect to the x axis. These components are combined with the x component to yield the angle of the fringes.

The price to be paid for automation is a substantial increase in the computation time. In our configuration, the determination of one component requires 45 s. It should be pointed out that the computer used in this work has limited performances;the time required will be considerably shorter when connection with a larger computer equipped with an array processor will be operational. Note that g(u) could be computed by Fourier transforming the weighted average of the power spectra of each line. However, the autocorrelation algorithm can easily be written in compact form in assembly language. For a reduced number of points as in the present case, direct computation of

of the autocorrelation is faster than the FFT algorithm.

Another shortcoming of the autocorrelation technique is the difficulty to measure the velocity when the fringe density becomes too low (less than five bright fringes, including the central one). In this case, the velocity can often be evaluated by the interactive one dimensional averaging method. So, the two methods are complementary.

5. ACCURACY OF THE TECHNIQUE

The overall accuracy of the technique depends on the accuracies which can be achieved in the photographic procedure and processing techniques.

5.1 Photographic procedure

Let us first consider the photographic procedure. The sources of error are the lens aberrations and the limited film resolution, causing the position of a particle to be recorded with an inherent error, and the spurious contributions on the in-plane movement recording by the out-of-plane motion.

5.1.1 Influence of the out-of-plane motion

In section 2.2 we referred that out-of-plane movement was a severe limitation on the use of true speckle in fluid dynamics applications. The reason for this limitation was that a slight out-of-plane movement by the scatterers resulted in two non-identical shifted speckle patterns poorly correlated. To cope with this problem, in the present technique, the particles are directly imaged and recorded as opposed to true speckle. However, as it will be shown in the following, out-of-plane movements may also contribute to errors in the velocity measurement.

Let us consider the imaging system for figure 12 and the particle in position P_1 within the laser sheet. Between exposures the particle moves to a position M_1 due to three dimensional fluid motion. The components of the displacement are dx_1, dy_1, dz, with $dx_1 dy_1$ being the in-plane and dz the out-of-plane components of the displacement. In the image plane, the photographic plate records the positions of the particle at P_2 and M_2. The coordinates of these points are given by :

P_1	M_1
$-Mx$	$-M(x+dx)(1+\frac{dz}{d_1})$
$-My$	$-M(y+dy)(1+\frac{dz}{d_1})$
d_1+d_2	d_1+d_2

(31)

where second order terms have been neglected for simplicity.

The displacement P_1M_1, measured by means of Young's fringes is given by

$$dx_m = M \cdot dx \left(1 + \frac{xdz}{dxd_1}\right) \qquad dy_m = M \cdot dy \left(1 + \frac{ydz}{dyd_1}\right) \tag{32}$$

The measured displacement components referred to the object plane are

$$dx_0 = \frac{dx_m}{M} = dx + \frac{xdz}{d_1} \qquad dy_0 = \frac{dy_m}{M} = dy + \frac{ydz}{d_1} \tag{33}$$

The contribution of the out-of-plane displacement to the measured displacement is given by two parasite terms $\frac{xdz}{d_1}$ and $\frac{ydz}{d_1}$. The error produced by the out-of-plane motion while negligible in the neighborhood of the optical axis, increases linearly, and may become important with the distance from the optical axis. The influence of the out-of-plane motion becomes particularly important when imaging the flow with short focal and wide objectives.

A relation can easily be found for the theoretical error in a measurement due to out-of-plane motion :

$$\epsilon_x = \frac{dx_0 - dx}{dx} = \frac{dzx}{dxd_1} = \frac{dz}{dx} \tan\varphi_x \tag{34}$$

$$\epsilon_y = \frac{dy_0 - dy}{dy} = \frac{dzy}{dxd_1} = \frac{dz}{dx} \tan\varphi_y$$

φ_x and φ_y are semifield angle components along the x and y axis respectively. Hence the error depends only on the ratio of the out-of-plane to the in-plane component of displacement and the tangent of the semifield angle.

Figure 13 shows the theoretical relative error for various ratios of $\frac{dz}{dx}$ and $\tan\varphi_x$.

5.1.2 Correction for out-of-plane motion

Analysis of figure 14 shows that in applications were large fields of view are involved (large magnifications and short focal length) and there are considerable out-of-plane motions, the errors in the measurement of the in-plane components may become important. This fact stresses the necessity for the implementation of techniques aiming at the elimination of the out-of-plane influence in the measurement. Here we present a technique which has been developed in the metrology of body displacements using white light speckle photography by Jacquot and Rastogi (Ref. 11). This technique although developed specifically for white light speckle photography, can be generally applied to coherent speckle photography or particle multiple exposure techniques, since the motion of speckle grains or particles are governed by the same geometrical laws.

The principle of the method consists of imaging a point, P_0, in the illumination sheet in two distinct directions as shown in figure 14 and recover its position in three dimensional space by stereoscopic like considerations.
Consider figure 14 and the point P_0. Its position can be restored from its two images P_1 and P_2 by tracing back the two lines P_1L_1 and P_2L_2 to their intersection. The individual displacements P_1M_1 and P_2M_2 can be measured by the Young's fringe analysis method and provided that the direction of the

displacement is known, the intersection of the lines M_1L_1 and M_2L_2 gives the point $M_0(x+dx, y+dy, dz)$. Therefore, using this method it is possible to retrieve the three components of the displacement.

A practical optical setup presented in reference 11 uses two viewing objectives arranged parallel and decentred with respect to the optical axis. This method is denominated 'Lateral decentring method'. The objectives are decentred respectively by $(\delta x,\delta y)$ for L_1 and $(-\delta x, -\delta y)$ for L_2. The relations governing the measured displacement components become

$$\begin{aligned} dx_{1_m} &= dx + \frac{dz}{d_0}(x+\delta x) \\ dy_{1_m} &= dy + \frac{dz}{d_0}(y+\delta y) \\ dx_{2_m} &= dx + \frac{dz}{d_0}(x-\delta x) \\ dy_{2_m} &= dy + \frac{dz}{d_0}(y-\delta y) \end{aligned} \qquad (35)$$

which yields, for the displacement components,

$$\begin{aligned} dx &= \frac{x(dx_{2_m}-dx_{1_m})+\delta x(dx_{2_m}+dx_{1_m})}{2\delta x} \\ dy &= \frac{y(dy_{2_m}-dy_{1_m})+\delta y(dy_{2_m}+dy_{1_m})}{2\delta y} \\ dz &= \frac{d_0}{2\delta x}(dx_{1_m}-dx_{2_m}) \end{aligned} \qquad (36)$$

The displacement components can therefore be determined according to eqs 30 and using the values of dx_m and dy_m previously measured by the Young's fringe method.

The limitations of this method are that the maximum out-of-plane motion which is permissible is less than the illumination sheet width.

Accuracy considerations also show other method limitations. Neglecting measurement errors in the evaluation of δx and δy (decentring parameters), an error analysis yields for the errors in the computed displacement :

$$\frac{\Delta(dx)}{dx} \cong \frac{\Delta(dx)_m}{dx_m} \left(1+ \frac{x}{\delta x}\right)$$

$$\frac{\Delta(dz)}{dz} \cong \frac{\Delta(dx)_m}{dx_m} \left(\frac{x}{\epsilon_x \, \delta x}\right) \qquad (37)$$

Equations 37 show that the errors are minimized for small $\frac{x}{\delta x}$. There is a practical limit in the upper value of δx which is set by the aberrations of the lens.

The above described technique is just an example of a method of solution to remedy the influence of out-of-plane motion. For each individual application different optical setups may be designed, having different performances. Nevertheless, it is important to keep in mind that these methods do not provide compensation for out-of-plane motion which is larger than the illumination sheet thickness.

5.2 Accuracy of the processing techniques

The accuracy of the methods described in chapter 4 can be evaluated in a simple way. Because it is extremely difficult to produce experimentally a fluid flow whose characteristics are known with an accuracy better than 1%, it was necessary to perform measurements in an artificial uniform velocity field. A suspension of latex particles (6 μm diameter) is photographed with 0.7 magnification. A uniform displacement field is obtained by reproducing the negative at unit magnification with a lateral

shift between two successive exposures. A large number of points of this photograph are analyzed by means of the above techniques in order to obtain statistical information about the experimental errors.

It is important to note that the measurement errors are due to the speckle present in the fringes. Since this speckle is the result of the random distribution of independent particles located in the illuminated region, the velocity evaluation must be viewed as the measure of a random variable. In the absence of systematic bias (sufficiently large fringe density), the standard deviation of the distribution is an estimate of the mean measurement error. When analysis is performed using a 0.5 mm diameter beam, the maximum measurable displacement is ~200 μm. Beyond this value the contrast of the fringes decreases strongly. For a 200 μm displacement, a sequence of sixty measurements is performed at different points of the photography. Analysis by the two techniques yields the same mean value (0.25 μm mean difference) with a nearly equal standard deviation of 2.5 μm (1.25% of the maximum displacement). The same values are obtained for a displacement of 150 μm. This mean error can be significantly larger than the inaccuracy quoted in solid mechanics (relative error $< 1\%$). This can be explained by the fact that, due to the absence of a classical speckle on the photograph, the shape of the diffraction halo can be distorted and so contributes to the measurement error. On the other hand, the optical Fourier transform performs a two dimensional correlation between two successive images of the same particles. However, given the limited resolution of the film, these images are not absolutely identical. Because of the low intensity of light that impinges on the film, the latter must be of high sensitivity (Kodak 2415 instead of holographic plates). That images of the particles cannot be compared with a precision higher than 2.5 μm may be due to the limited resolving power over such a film (320 lines/mm).

6. APPLICATIONS

6.1 Measurement of a low velocity convection flow in a cylindrical Rayleigh-Benard cell

The Rayleigh-Benard cell (shown in Fig. 15) consists of two cylindrical copper discs separated by a glass cylinder which constitutes the lateral wall of the cell (Ref. 6). The aspect ratio (diameter vs height) is 2.0. This assembly is contained in a parallelipipedic box whose lateral walls are made of glass plates. Both the inside and the outside of the inner cylinder are filled with glycerol. The matching between the refractive indices of glycerol and glass prevents dioptric effects which would introduce severe aberrations. The temperature difference between the two horizontal copper surfaces is regulated by temperature-controlled water flows. In this geometry, the flow pattern arising at the critical Rayleigh number consists of one roll of cylindrical symmetry (Ref. 6). This convection torus remains steady for moderate temperature differences (in our case, $\Delta T/\Delta T_c = 1.66$).

The beam from an argon laser (1.7 W at 514.5 nm) is focused in a vertical plane containing the cell axis. A mechanical chopper produces 10 pulses (each of 20 ms duration) separated by 3 s intervals. The beam illuminates the diffusing particles (with 5.8 μm diameter) suspended in the fluid contained in the inner cylinder. The picture obtained from a camera focused on the illuminated plane is similar to those obtained in conventional tracer methods (see Fig. 16a).

It should be noted that an incoherent light source could be used, however, laser light provides high power densities in a well defined and thin plane. Note also that, due to the Gaussian profile of the focal line, the intensity of the light diffused by the particles can strongly vary, inducing non-uniformity in the shapes of the images of the particles. However, it is observed that this effect does not affect the final results. Therefore, particle monodispersity is not a crucial factor in such an experiment.

The photograph shown in figure 16a has been analyzed using the spatial filtering setup of figure 5. Figures 16b-f show isovelovity fringes obtained by displacing the filtering hole vertically (Figs. 16b-e) or horizontally (Fig. 16f). These isovelocity maps allow a rapid wholefield examination of the features of the flow pattern. For instance, one observes that the vertical velocity in the vicinity of the cell axis is much larger than near the cell wall. This is quite obvious because the particles descending near the wall must ascend near the axis and therefore because of mass conservation, the velocity must be larger in the vicinity of the center of the cell.

Figure 17 shows the vertical velocity component measured along a horizontal line at mid height of the convection cell. The velocity measures have been obtained using both analysis techniques : processing of the Young's fringes produced by point-by-point scanning of the photograph and analysis of the position of the isovelocity fringes drawn by spatial filtering. The comparison between the two sets of data shows a satisfactory agreement.

6.2 Vortex flow

Another example of application of a multiple exposure technique in a liquid flow is presented. The flow consists of a vortex ring generated by a pulsating jet. This experiment was carried out at Lockheed International Research Institute (Ref.12).

The experimental apparatus is sketched in figure 18. The vortex rings are generated in the following manner. A solenoid excited by a pulse train provides a pulsating pressure supply which drives the water from the seeded water reservoir into the discharging tank through a nozzle with 12.5 mm in diameter. The flow Reynolds number was about 500, with a velocity of the jet at the exit of about .8 m/s. For the sake of high contrast in flow visualization, the seeding concentration in the reservoir and in the discharging tank were different. The seeds used in most of the testing were titanium dioxide particles having a diameter ranging 10-50 microns.

A CW argon-ion laser delivering 7 watts in the 5145 Å wavelength with a Bragg cell as a shutter was used to produce the pulsed light sheet. The Bragg cell arrangement is shown in figure 19. The advantages of the use of a Bragg cell as a shutter are the possibility of an independent choice of the number of illumination pulses, the time between pulses and the pulse duration. The Bragg cell is triggered by the phase lagged output of the pulse generator, which permits it to lock the vortex structure at any phase of its development. The viewing and recording optics consists of a camera with a 100 mm objective and maximum aperture corresponding to F# 3.5. The magnification for the recording was 1.5, and the film used was a Kodak Royal X ASA 1250.

Figure 20 is a multiple exposure photograph (4 exposures) showing a lateral view of a longitudinal cut of the vortex ring. The time between laser pulses was 1 ms and the pulse duration .05 ms. As in conventional flow visualization techniques, the photograph shows the boundaries of the seeded regions which provide the streakline information. The novel aspect is on the information contained by the particle images, which provide the streamlines, in the limit of short duration between laser pulses. Figures 21a-b show top views of transversal cuts through the center of the vortex ring, at different stages of its development. Comparison of these photographs shows evolution and growth of instabilities (Widnall) leading to the formation of small vortices (Fig. 21b).

These photographs also document the remarkable differences between streaklines and streamlines in unsteady and perturbed flow.

Using the interferometric methods described herein a small portion of the photographic negative of figure 20 was analyzed and the local velocity vectors derived. Results are presented in figure 22 which displays the velocity vectors overlayed in the corresponding locations in the photograph.

6.3 Application to the study of the transition region of a gas round jet

To demonstrate the capabilities of speckle velocimetry for the study of gas flows, we have chosen to study the transitional region of an unexcited round jet (diameter : 20 mm) at a low Reynolds number (Re=2.300) (Refs. 8, 13). Although studies of axisymmetric jets are usually performed at higher Re, this flow exhibits a well defined sequence of characteristic events: rollup of unstable vortices near the nozzle, interaction of these vortex rings by pairing, and appearance of smaller scale turbulence when the paired large scale structure aprroaches the end of the potential core. The boundary layer at the nozzle is laminar, the mean velocity profile agreeing very well with the Blasius profile. The momentum thicknes of this exit profile is 0.35 mm and the shape factor is 2.65. The free stream turbulence measured on the axis is of the same order of magnitude as the noise of the hot wire velocimeter (less than 1%). The instability of the shear layer (momentum thickness measured at x/D=0.25 : 0.43 mm) gives birth to vortex rings near x/D=1, but with an important jitter in the rollup location, growth rate, and convection velocity. The power spectrum of the signal of a hot wire velocimeter located at x/D=1, y/D=0.5 shows a well defined peak at 55 Hz with a half height width of about 4 Hz. The Strouhal number (St_θ) based on the mean frequency and on the momentum thickness is 0.014. This agrees satisfactorily with the 'classical' value for spatial instability of a tanh(y) layer (St_θ=0.0165). However, it must be noted that the Strouhal number (St_D) based on the diameter of the jet is 0.64, which approaximates the Strouhal number on the 'jet-column' mode (St_D=0.85) found in excited jets at higher Re.

The experimental setup is shown in figure 23. The beam from a double pulsed ruby laser (delay between the 30 ns pulses : 150 μs) is focused with a system of spherical and cylindrical lenses in a plane containing the axis of the jet. The air flow is seeded with micron sized oil droplets generated with a conventional blast atomizer. Part of the air flow from the aerosol generator is diverted and injected in the ambient atmosphere with

a very low velocity. This secondary seeded flow allows us to measure the velocity distribution of the entrained fluid. Great care has been exercised to prevent any disturbance in the jet instability. A double exposure image of the droplets is recorded (on Kodak 2415 film) at a magnification of 0.8 with a camera focused on the illuminated plane. The maximum displacement of the images of the droplets is about 250 μm. The photographs are analyzed point by point by illuminating a small region (diameter 0.6 mm) with a focused laser beam and analyzing the Young's fringes using the digital processing setup described in chapter 4.

Figure 24 shows a photograph of a vortex ring whose center is located 2.4D downstream of the jet nozzle. It must be noted that only one side of the ambient atmosphere is seeded with oil droplets and that the droplet concentrations are different. This allows for discrimination between the jet fluid and the entrained fluid. The laser pulses are synchronized with the arrival of the roll by using the signal of a hot wire velocimeter located at the point where the mean velocity is about $U_e/2$ in the rollup region (x/D=1). This signal is processed to produce a triggering pulse which is delayed to take into account the time interval between the detection of a vortex ring and its arrival in the region to be photographed. In the case of figure 24, the delay is 36 ms.

Figure 25a shows the in-plane velocity field of the roll as viewed in a referential moving with the velocity of the geometric center of the roll (U_c=0.55 U_e, where U_e is the exit velocity). The two dimensional velocity field is measured on a square mesh (step of 0.5 mm on the photograph). This regular disposition allows the spatial derivatives of the velocity to be estimated by a simple algorithm. For example, if the locations of the measurement points are labeled with thr indices i and j, the derivative $\partial u/\partial y$ at location (i,j) is proportional to

$$\frac{\partial u(i,j)}{\partial y} \propto \frac{1}{2}\left(u(i,j+1)-u(i,j-1)\right) \qquad (38)$$

For the boundaries of the velocity field, where this scheme cannot be applied, the velocity of the point itself is subtracted from the velocity of the nonzero neighbor. The resulting decrease in accuracy will be illustrated in the vorticity maps, where occasionally contours surround isolated boundary points. Labeling of these contours will often be omitted. Figure 25b shows isocontours of the vorticity $\Omega = \frac{\partial v}{\partial x} - \frac{\partial u}{\partial y}$. It is important to note that the curves drawn in figure 25b represent unsmoothed experimental data. Obviously, the algorithm of equation 38 is very sensitive to experimental errors. A simple error computation based on the previously quoted inaccuracies shows that the mean uncertainty on the vorticity is about 15% of the maximum value. Nevertheless, velocity measures are accurate enough to check that the entrained ambient fluid is irrotational (see figure 25).

By increasing the time delay it should be possible to photograph the vortices farther downstream, but this procedure fails because of the interactions between successive rolls which produce important variations in the convection velocities. However, it is still possible to detect the arrival of a paired structure if the hot wire is located on the axis in the interaction region. The laser is triggered on the positive peaks of the derivative of the hot wire signal. This allows for the detection of a structure before its center reaches the wire. Note that, due to the interaction, the mean frequency of the velocity is halved. At this distance from the nozzle, the Strouhal number St_D is 0.32. Figure 26 shows a typical pairing event with the hot wire (apparent on the photograph) located near x/D=3.5. Two rolls are apparent on the photograph : the 'slow' roll which has expanded and decelerated, and the 'fast' roll which, after stretching and acceleration, tends to overtake the preceding vortex ring in a "leapfrog" motion. The differential velocity between the two vortices can be estimated by considering figure 27 where a constant velocity of abour 0.44 U_e has been subtracted. It must be pointed out that a convection velocity can hardly be assigned to the fast roll because of the

large elongation of this vortex. This agrees with the conclusions found at higher Re where it has been proved that the Taylor hypothesis works very well for isolated structures, but fails when interaction takes place. In this case no satisfactory convection velocity can be found. It can be observed in figure 27b that the vorticity of the inner part of the fast roll decreases during its stretching motion due to viscous dissipation. This effect can also be explained by noting that for axisymmetric motions the Euler equation reduces to $\frac{d}{dt}\frac{\Omega}{R} = 0$, where $\frac{d}{dt}$ denotes the material derivative and R is the distance from the axis. The inward motion of the fast roll is thus accompanied by a decrease in derivative.

The introduction of small scale turbulence during the pairing process prevents reliable real-time detection of the paired structure farther downstream if the derivative of the signal of the hot wire velocimeter is used. This derivative shows important peaks unrelated to the large scale structures. However, by using the peaks of the velocity signal itself, it is still possible to detect these structures. Figure 28 shows an example of structures detected near x/D=6. The velocity field, viewed in the laboratory referential, can be found in figure 29a. The vorticity contours are shown in figure 29b. It is important to note that some data are missing. These holes in the velocity field are due to the limitations of the technique : the decreases in fringe contrast when the velocity gradients are too high and when the out-of-plane velocity component is too important. Near the end of the potential core, these effects (especially the second one) occasionally prevent reliable measurement of the in-plane velocity. Further studies are needed to overcome this drawback. For example, if the gradient of the out-of-plane velocity is weak, thickening the illumination sheet would solve the problem (the thickness in this experiment is about 200 μm). The vorticity contours (and others not shown here to save space) show clearly the presence of small scale turbulence but also that the high vorticity regions are predominantly remnants of the 'fast' roll. Notwithstanding the fact that these rolls are difficult to discriminate in figure 28

REFERENCES

1. HAMA, F.R.: Progressive deformation of a perturbed line vortex filament.
Physics of Fluids, Vol. 6, No 4, April 1963, pp 526-534.

2. ELKINS, R.E. et al.: Evaluation of stereoscopic trace particle records of turbulent flow field.
Rev. Sci. Instr., Vol. 48, No 7, July 1977, pp 738-746.

3. KOBAYASHI, T.; ISHIHARA, T.; SASAKI, N. in
Proc. Int. Symp. Flow Visualization, Ann Arbor, Michigan, 1983, p. 261.

4. SIMPKINS, P.G. & DUDDERAR, T.D.: Laser speckle measurements of transient Benard convection.
J. Fluid Mechanics, Vol. 89, Part 4, 1978, pp 665-671.

5. MEYNART, R.: Equal velocity fringes in a Rayleigh-Benard flow by a speckle method.
Applied Optics, Vol. 19, No 9, May 1980, pp 1385-1386.

6. MEYNART, R.: Convective flow field measurement by speckle velocimetry.
Rev. Phys. Appl., Vol. 17, Mai 1982, pp 301-305.

7. MEYNART, R.: Instantaneous velocity field measurements in unsteady gas flow by speckle velocimetry.
Applied Optics, Vol. 22, No 4, Feb 1983, pp 535-540.

8. MEYNART, R.: Speckle velocimetry study of vortex pairing in a low-Re unexcited jet.
Physics of Fluids, Vol. 26, No 8, August 1983, pp 2074-2079.

9. VAN DE HULST, H.C.: Light scattering by small particles.
New York, Wiley; London, Chapman, 1957.

10. Tables of scattering functions for spherical particles.
US Dept. of Commerce, Appl. Maths Series 4.

11. JACQUOT, P. & RASTOGI, P.: Influence of out-of-plane deformation and its elimination in white light speckle photography.
Optics and Laser in Engineering, Vol. 2, 1981, pp 33-55.

12. LOURENÇO, L. & WHIFFEN, M.C.: Laser speckle method in fluid dynamics.
Paper to be presented at the 2nd Int. Symp. on Application of Laser Anemometry in Fluid Mechanics, Lison, Portugal, July 1984.

13. MEYNART, R.: Mesure de champs de vitesse d'écoulements fluides par analyse de suites d'images obtenues par diffusion d'un feuillet lumineux.
Ph.D. Thesis, U. Libre de Bruxelles, Belgium, October 1983.

because of the intricate mixing with the entrained fluid, the vorticity bearing regions near the trailing edge and near the high curvature leading edge can still be discerned. It must be pointed out that the peak values of vorticity are of the same order of magnitude as those observed in figure 25. Note that the mean vorticity of the outer roll cannot be very important because this region of the flow grows by engulfing potential fluid from the core.

It can be inferred from figures 28 and 29 and other images not shown here (Refs. 8, 13) that the shape, size and location of these "lumps" of vorticity can vary greatly from one individual realization to another. Because of this "phase jitter" a conventional conditional sampling technique would smear out these features and educe a larger vortical region with smaller peak value. It is the virtue of speckle velocimetry to provide this information which would be lost otherwise. In view of this the classical representation of a large scale structure in a low Re jet must be reconsidered : the preturbulent unstable rolls give birth to vortical "pumps" with important jitter in shape, orientation and location. These high vorticity regions are embedded in a larger low vorticity structure and true random turbulence must be added to complete this description.

LIST OF FIGURES

1. Layout for speckle photography
2. Fringe analysis setup
3. Fringe width vs number of exposures
4. Two dimensional Fourier transform of aligned point sources
   (a) Two-point sources; (c) Six-point sources;
   (b) Four-point sources; (d) Eight-point sources
5. Spatial filter
   L_1, L_2 : beam expander L_3, L_4 : transform lenses
   P : photograph I : image plane
   FP : Fourier plane with the mask;
6. Interference fringes
   (a) From photographic negative ; (b) From photographic positive
7. Working diagram
8. Layout of VKI Image Processing
9. Fringe processing system
   L_1, L_2 : lenses for beam diameter adjustment
   P : photograph
   L_3 : Fourier transform lens
   F : Fourier plane with stop for undiffracted beam
   C : video camera
   A/D : video interface (see Fig. 8)
10. Photographs of TV monitor showing an example of processed fringes.
    Center of the photographs : luminous intensity I(m,n)
    (a) -A : intensity integrated parallel to the fringes f(m) $0 \leqslant m \leqslant 127$
        -B : log f(m)
        -C : |FFT f(m)|
        -D : |FFT log f(m)|
    (b) -A and C : see (a)
        -B : $k(m) = \{\log f(m)\} \cdot \sin^2 \pi m/127$
        -D : |FFT k(m)|
    (c) -A : Intensity integrated perpendicular to the fringes

11. Photograph of TV monitor for same fringes as in figure 10 processed using the autocorrelation technique

    A - averaged autocorrelation $g(u)$ $0 \leqslant u \leqslant 127$

    B - $g'(u) = g(u)/(1+\exp -u^2/p^2)$ where p is an adjustable parameter

    C - FFT $g(u)$

    D - $|\text{FFT } g'(u)|$

12. Imaging system

13. Theoretical relative error of in-plane component due to out-of-plane motion

14. Simultaneous recording on two photographic plates to measure the three components of displacement

15. Section through the axis of the convection cell

    A : Copper plates; C : Glass plates;

    B : Inner glass cylinder; D : Water inlets

16. A : Multiple exposure photograph of the convection flow

    B : Filtered image (the fringes are recorded with reversed contrast on a high γ film)
    Vertical velocity component, Δv_z = 15.5 µm/s

    C : Δv_z = 16.8 µm/s

    D : Δv_z = 20.6 µm/s

    E : Δv_z = 25.2 µm/s

    F : Horizontal velocity component, Δv_x = 18.8 µm/s

17. Vertical component of velocity measured along a horizontal line at mid-height of the convection cell

    • data obtained by analysis of the Young's fringes produced by point-by-point scanning of the photograph of figure 16a. The error bar ⊢ symbolizes the inaccuracy determined in § 5.2

    ⋆ data inferred from the position of the isovelocity fringes of figure 16b

18. Experimental apparatus for vortex flow experiment

19. Sketch of Bragg cell shutter

20. Multiple exposure photograph of a lateral view of a longitudinal cut of the vortex ring

    Top : original photograph (negative)

    Bottom : positive copy

21. Multiple exposure photograph of transversal cuts through the center of the vortex ring at different stages of its development

    A : early stage B : later stage

22. Velocity map of a part of figure 20

23. Experimental setup

    A : air flow G : aerosol generator L_2 : cylindrical lens

    B : beam from a double pulsed ruby laser L_1 : spherical lens L_3 : camera lens

24. Photograph of a vortex ring detected at x/D=1.
The geometric center of the vortex ring is located at x/D=2.4

25. A : In-plane velocity field of the vortex in figure 24
(the convection velocity is $0.55U_e$)

B : Vorticity contours Ω/Kf_p, where f_p is the rollup frequency (55Hz); K is equal to 2.09. The crosses denote the points located at the corners of the velocity field and the boundaries of the roll are drawn as dotted lines

26. Photograph of a typical pairing event. Note the hot wire velocimeter at x/D=3.5

27. A : Velocity field of the interacting vortices shown in figure 26
(the convection velocity is $0.44U_e$)

B : Vorticity contours Ω/Kf_p, with K = 2.35. Note that the boundaries of the rolls are drawn as dotted lines)

28. Photograph of a typical large scale structure detected using a hot wire located at x/D=6.04

29. A : Velocity field of the large scale structure shown in figure 28

B : Vorticity contours Ω/Kf_p, with K = 1.77. Note that some contours are qualitatively interpolated.

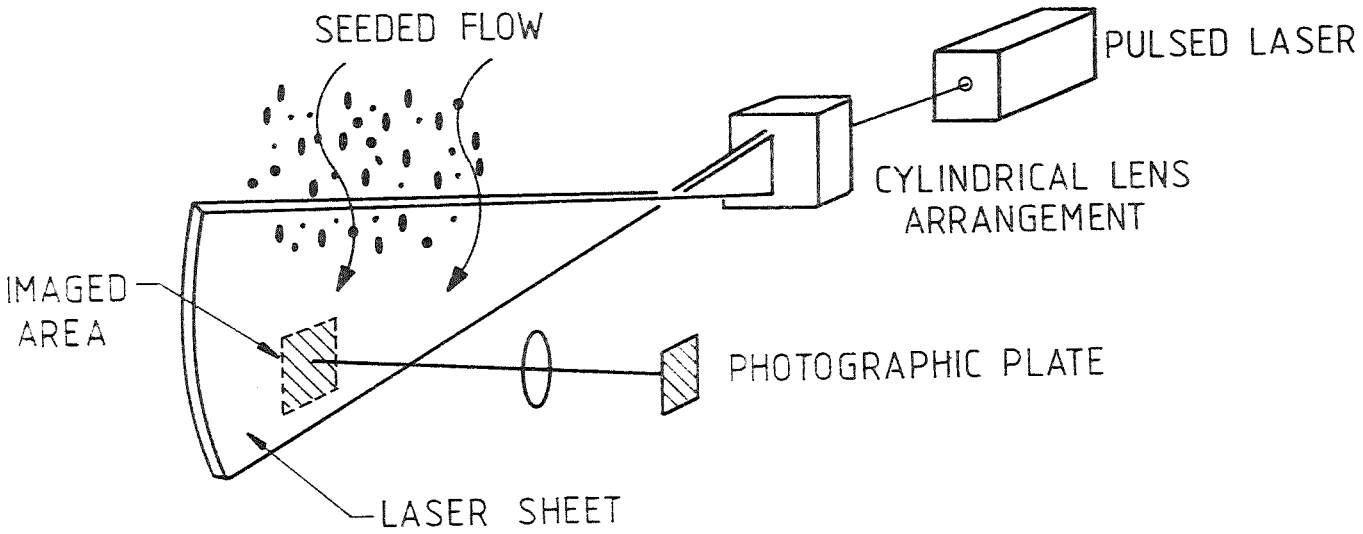


FIG. 1 - LAY - OUT FOR SPECKLE PHOTOGRAPHY

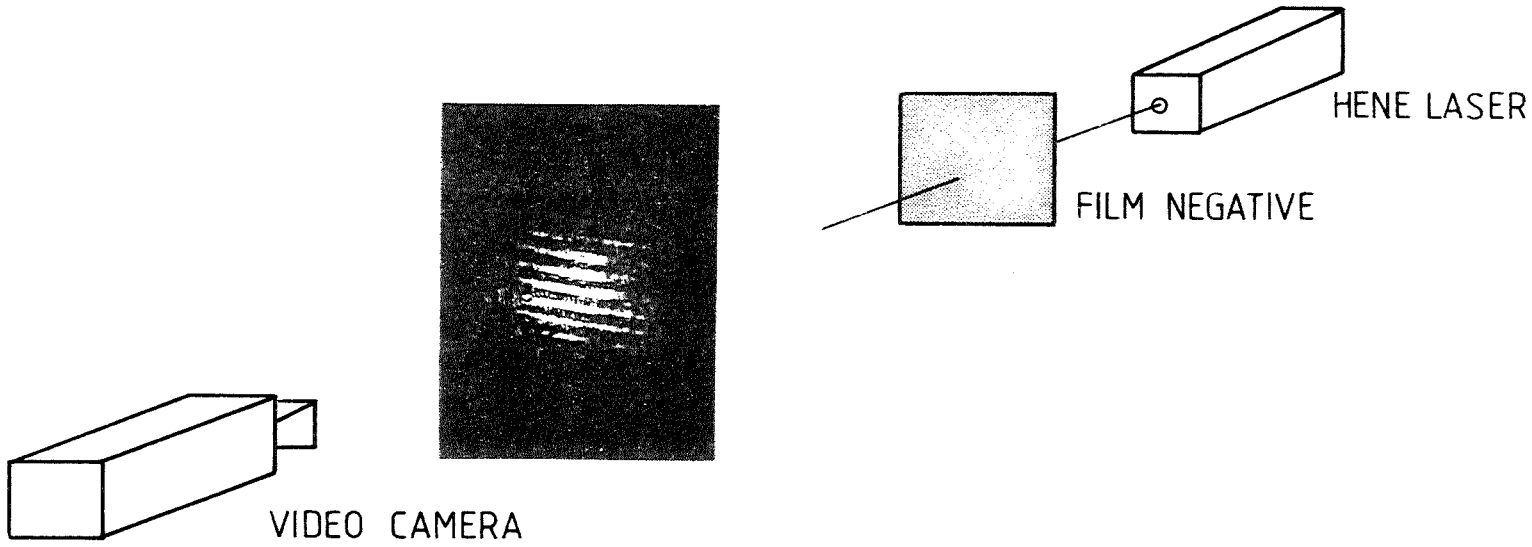


FIG 2 - FRINGE ANALYSIS SET UP

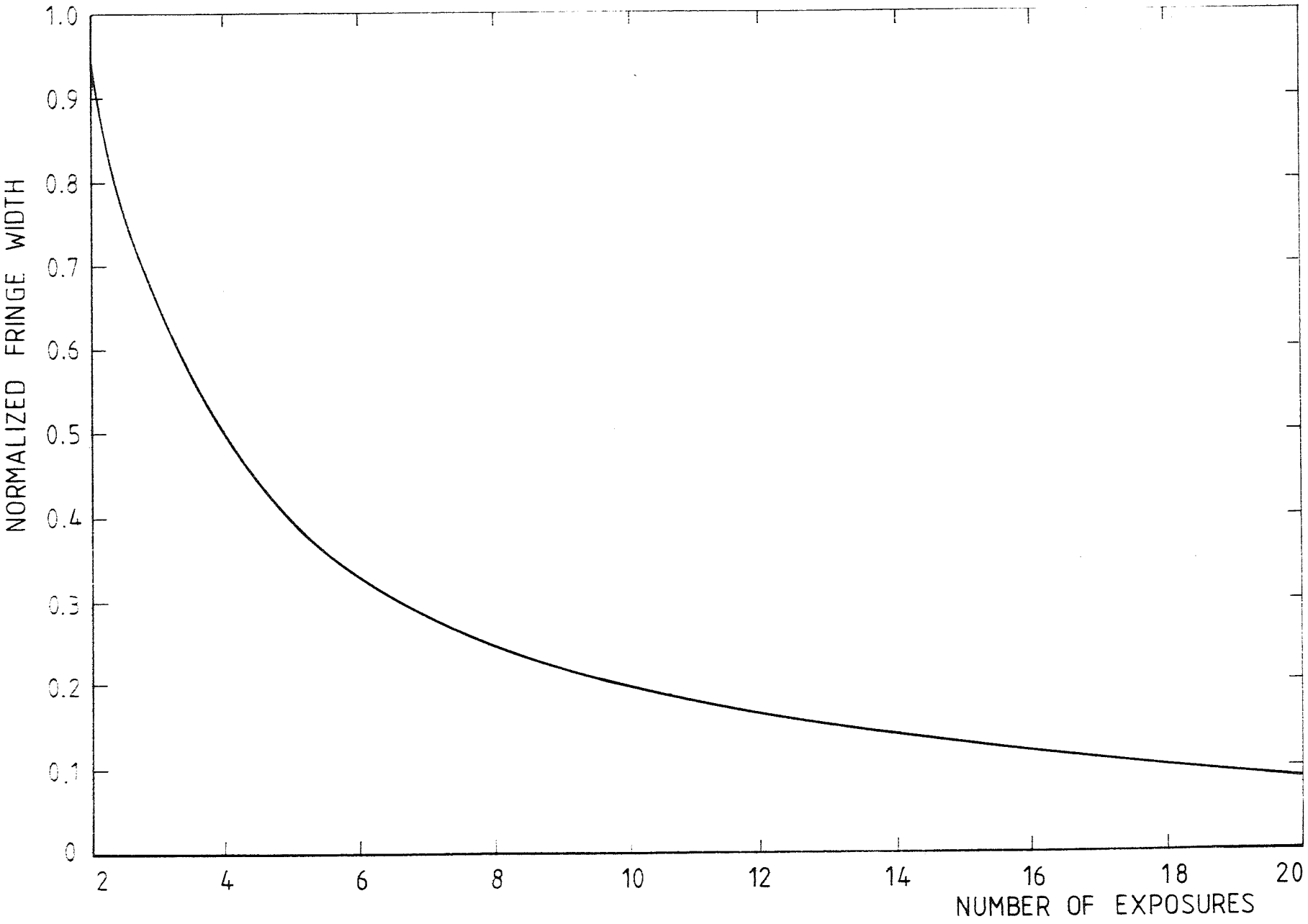
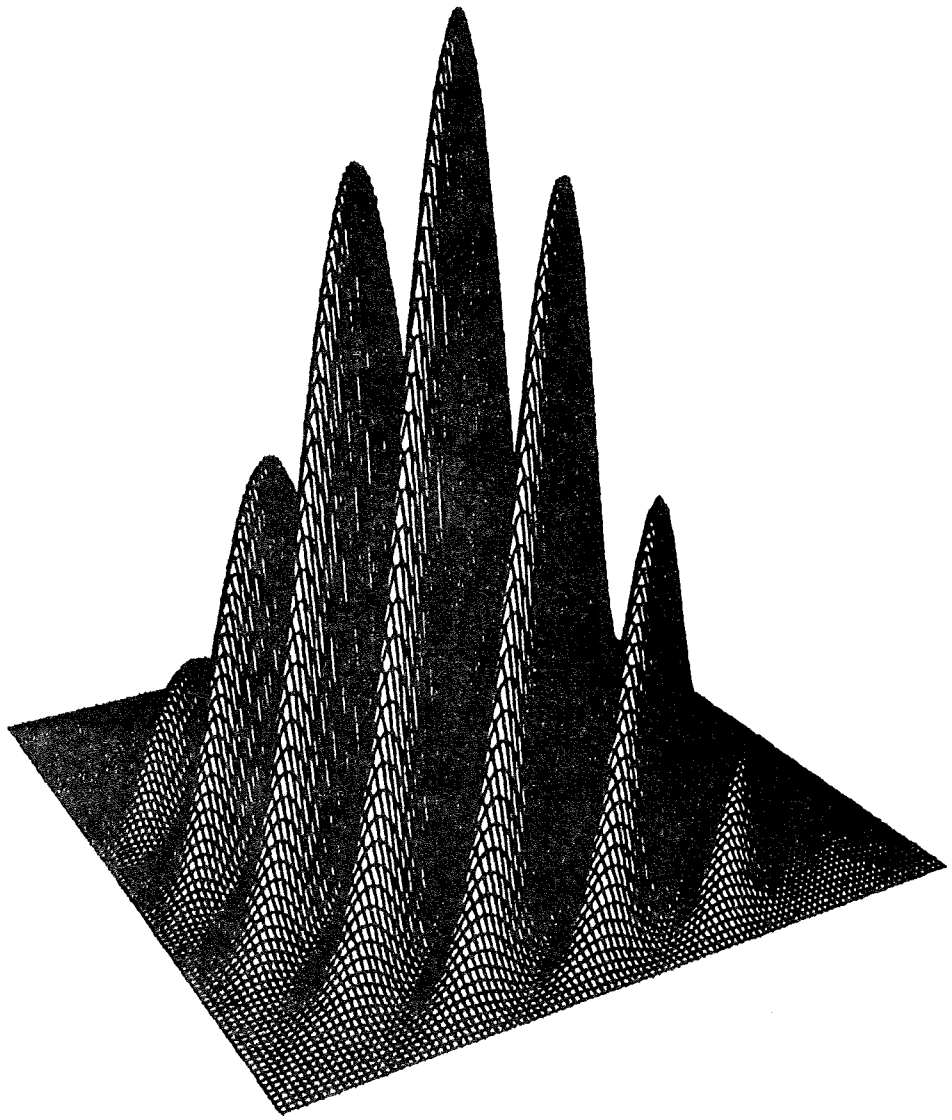
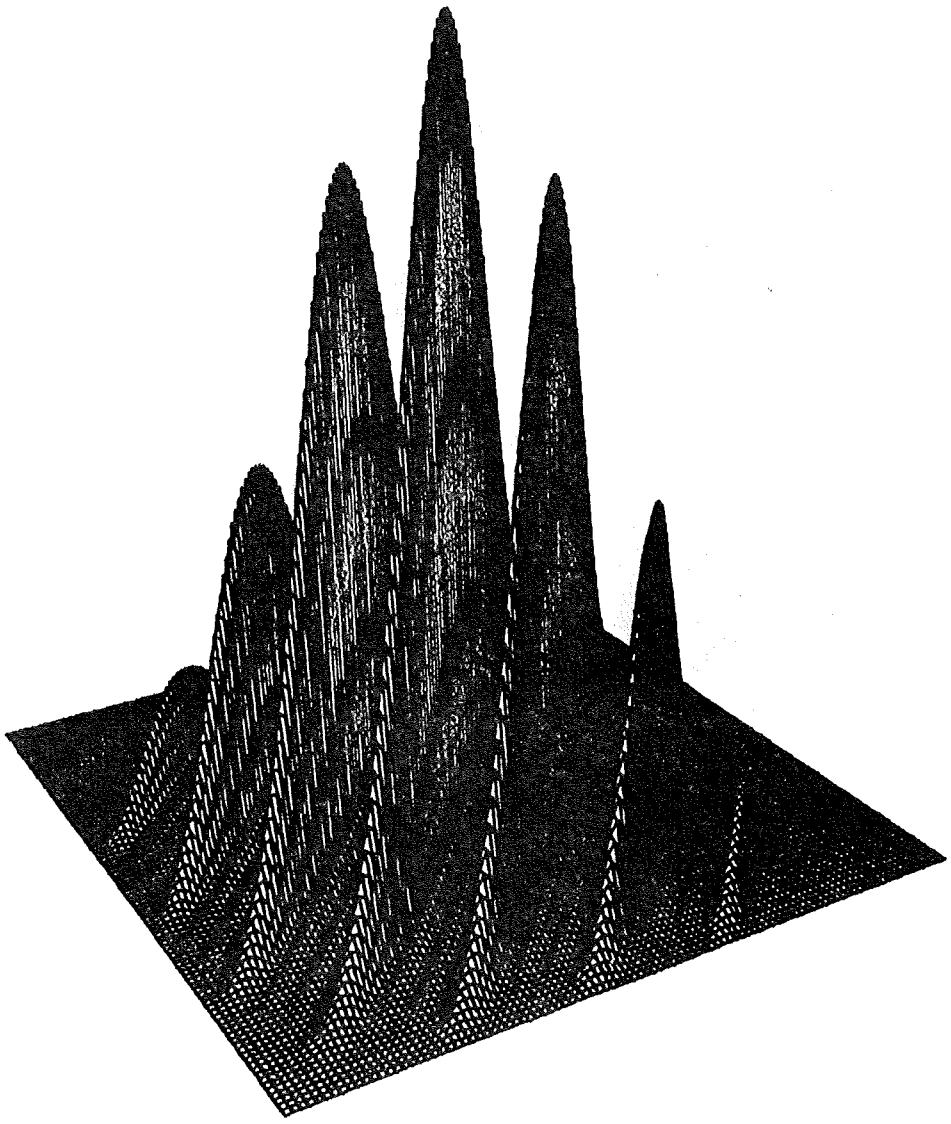


FIG. 3 - FRINGE WIDTH VERSUS NUMBER OF EXPOSURES



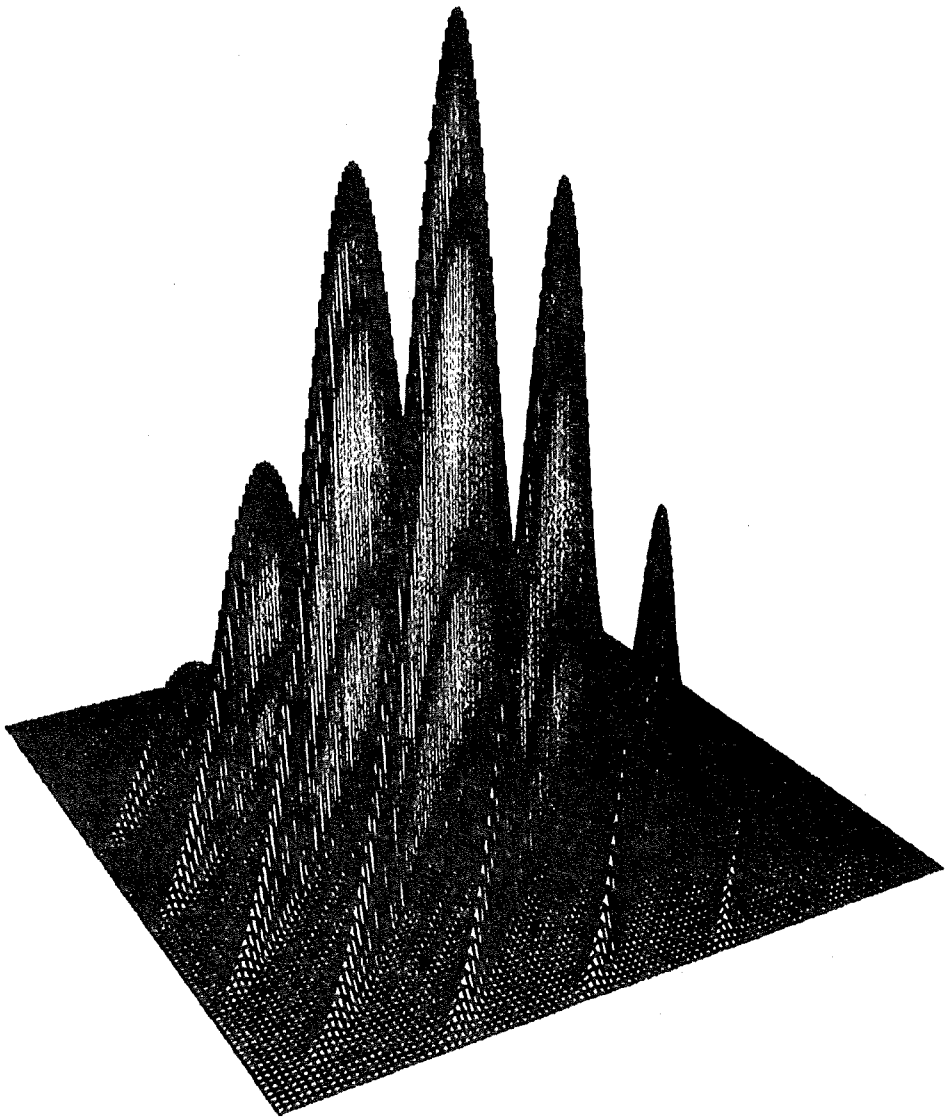
FFT OF ARRAY

FIG. 4 (a)



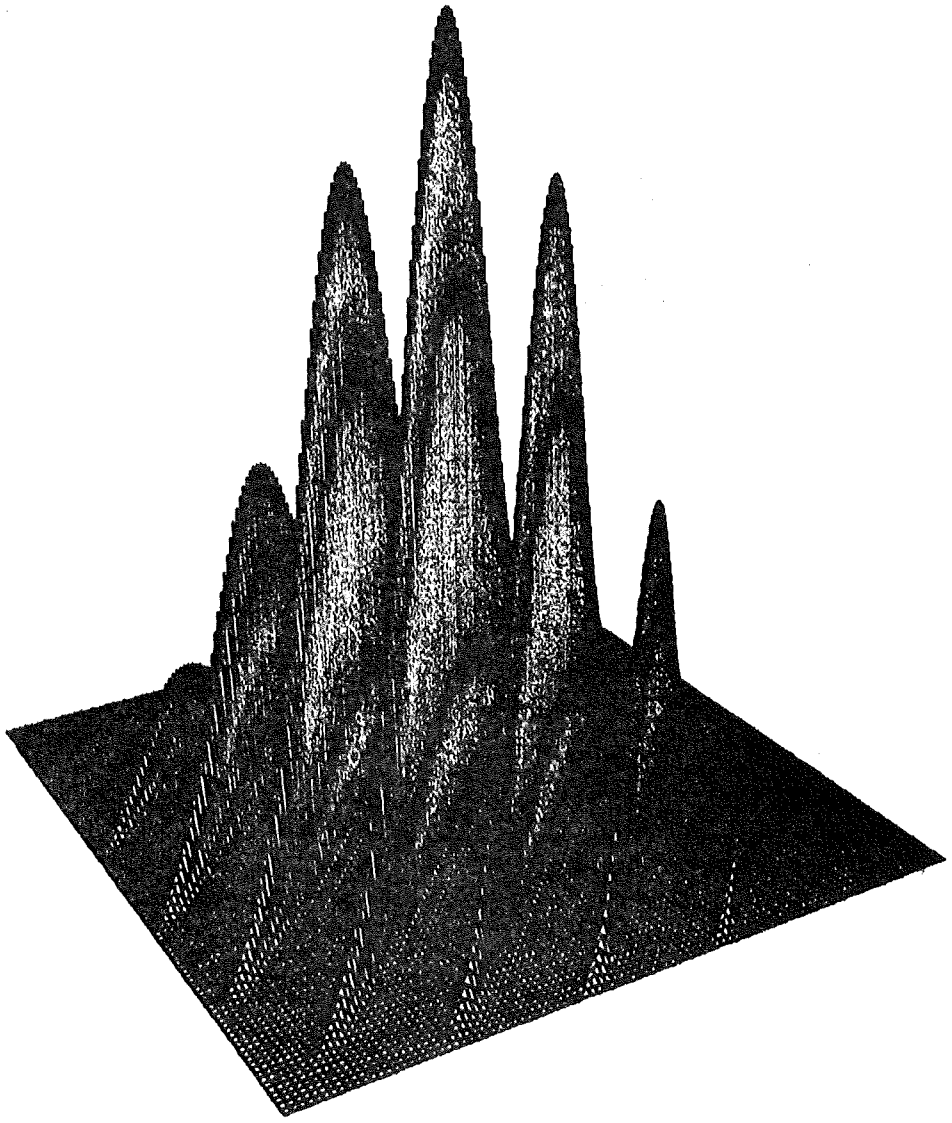
FFT OF ARRAY

FIG. 4 (b)



FFT OF ARRAY

FIG. 4 (c)



FFT OF ARRAY

FIG. 4 (d)

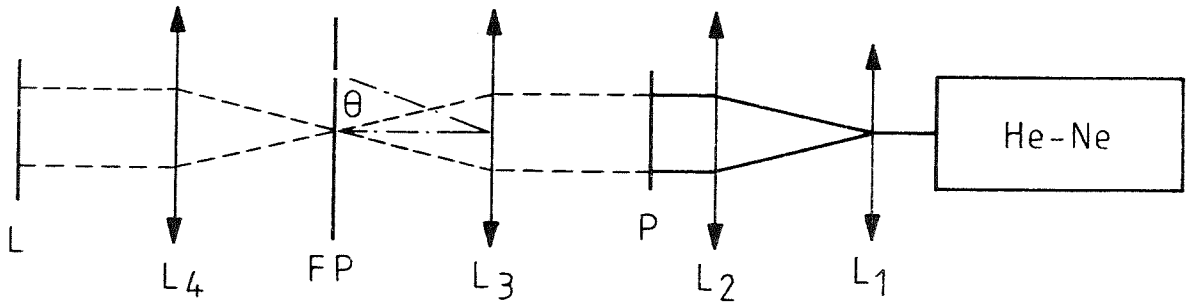


FIG. 5 - SPATIAL FILTER

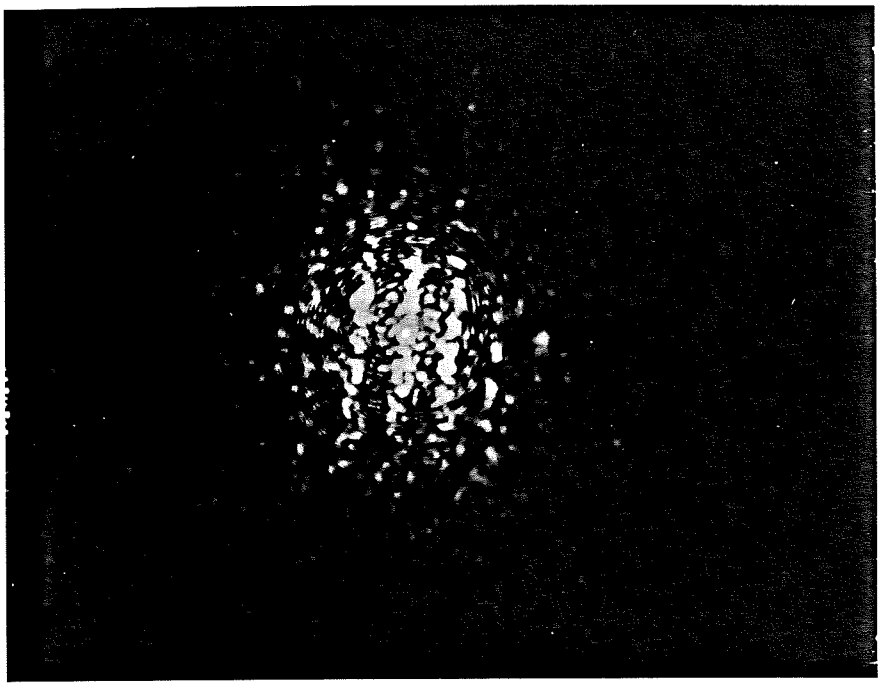
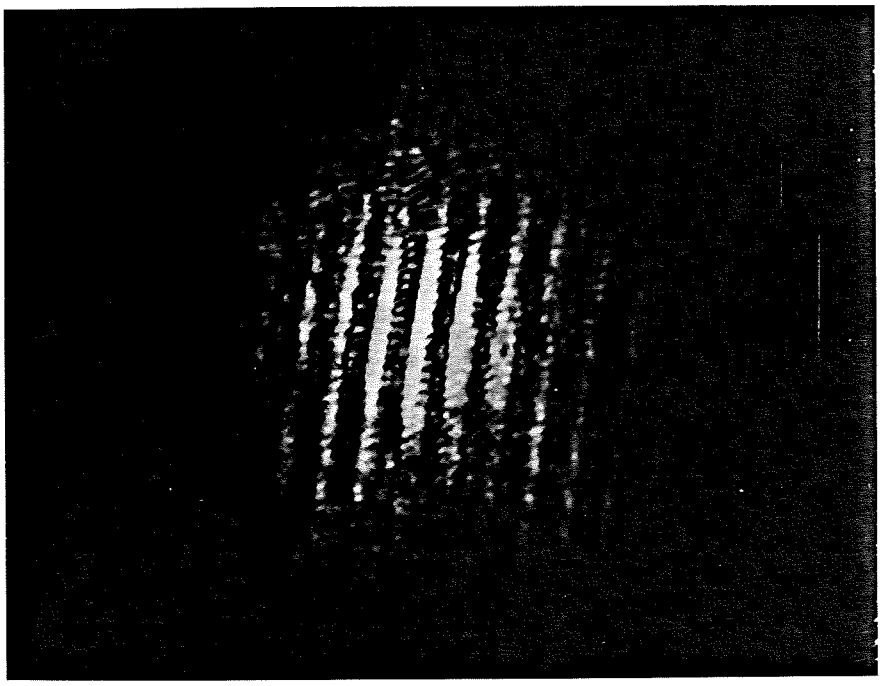


FIG 6a



6 b

YOUNG'S FRINGES

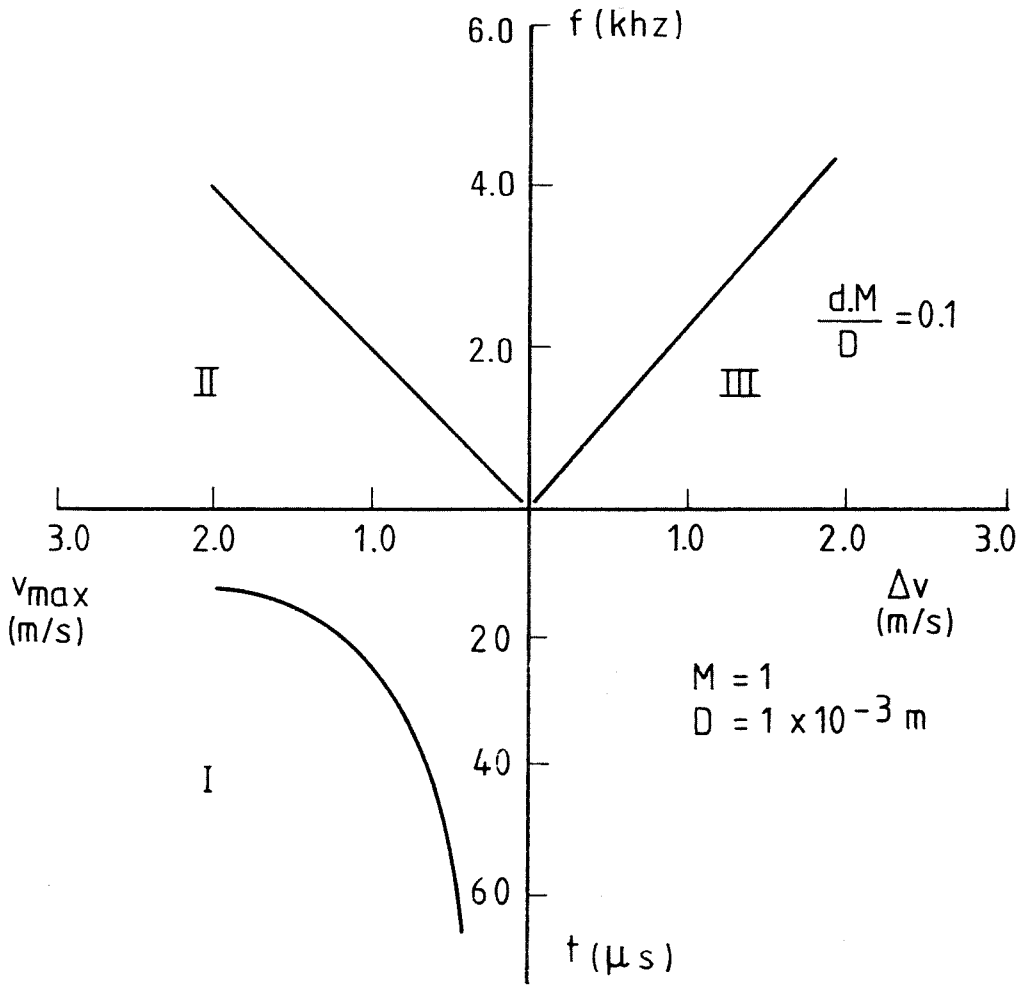


FIG. 7 - WORKING DIAGRAM

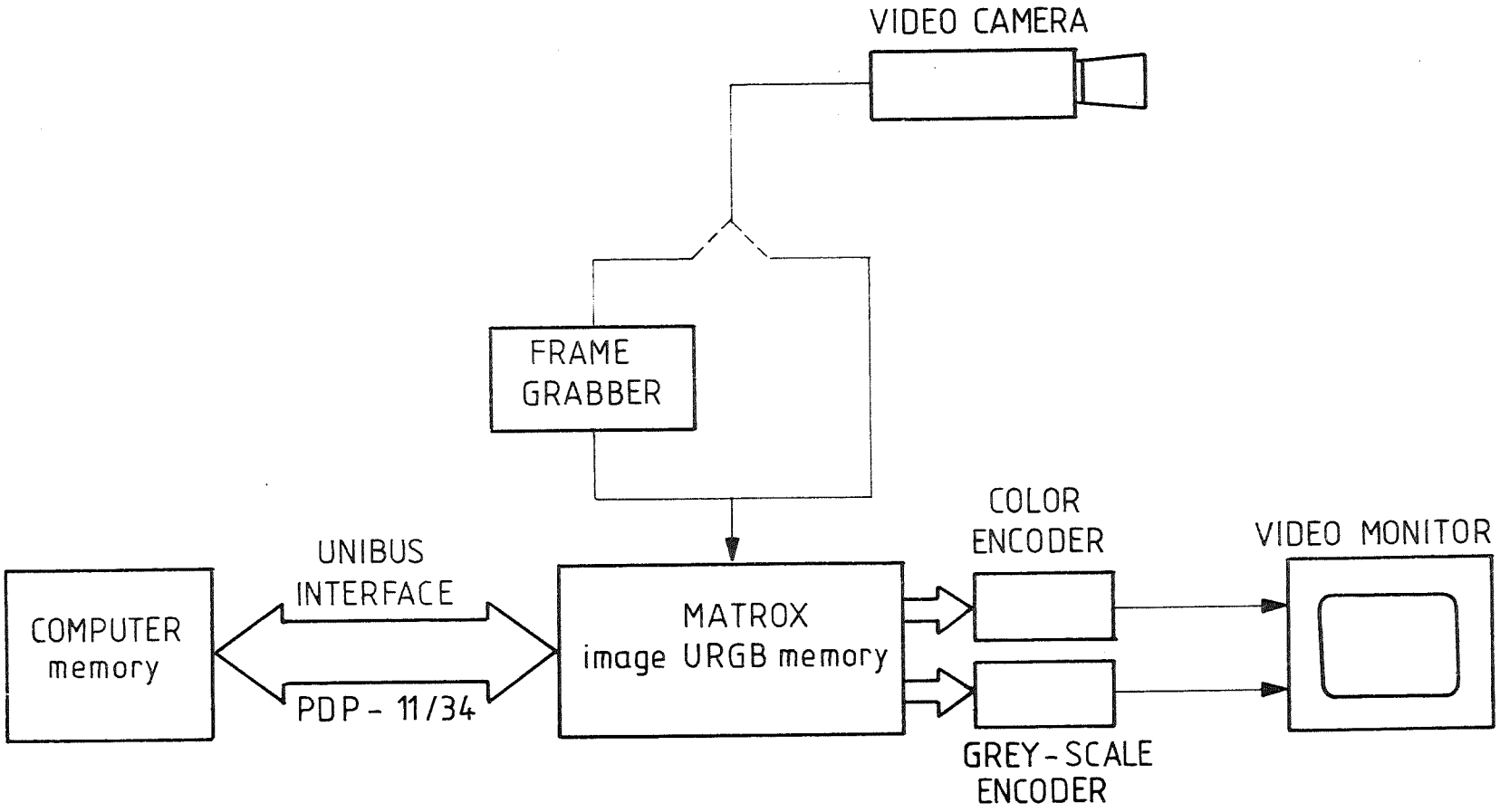
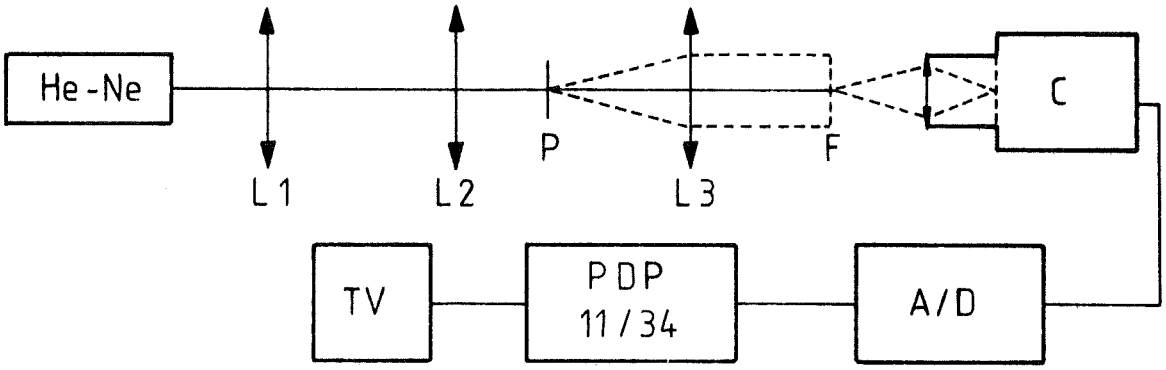


FIG 8 - LAY - OUT OF VKI IMAGE PROCESSING UNIT



FRINGE ANALYSIS SYSTEM

FIG. 9

A	B
C	D

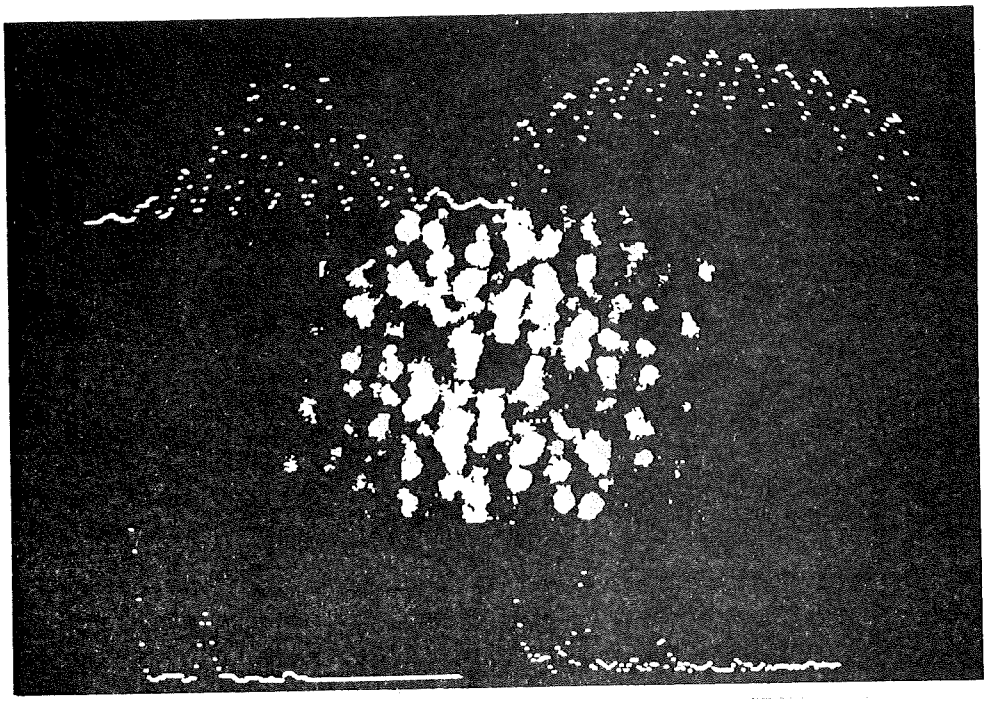
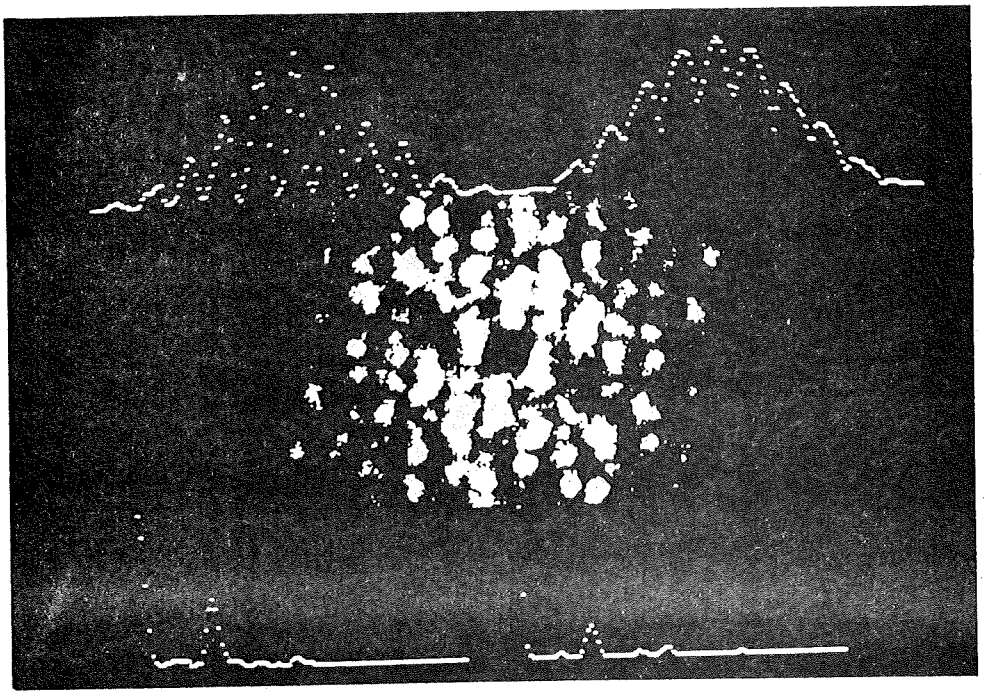


FIG 10a



10 b

EXAMPLES OF PROCESSED FRINGES

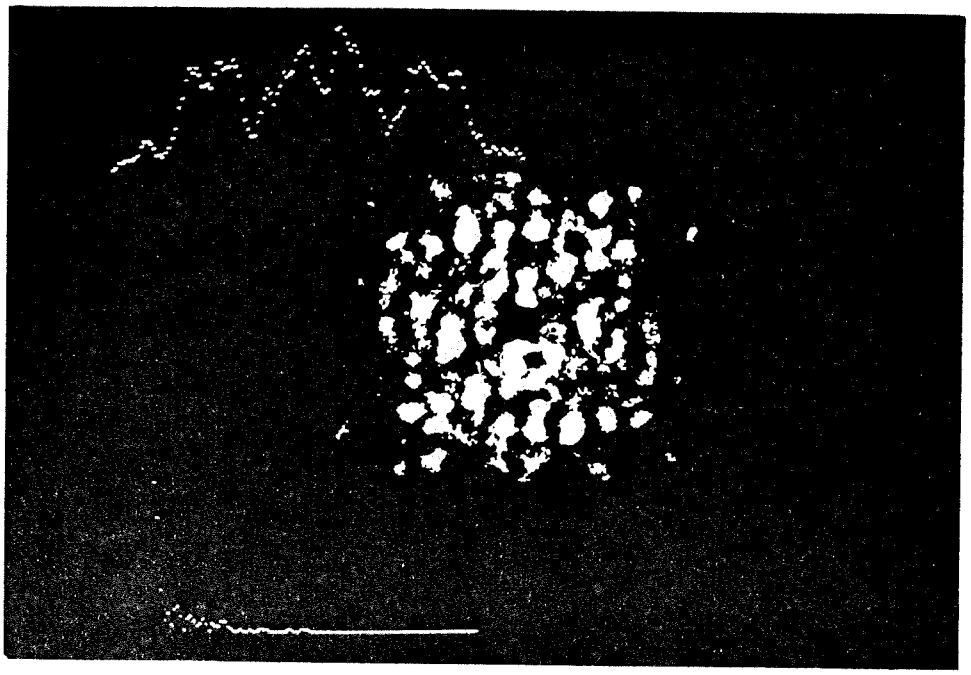


FIG 10c

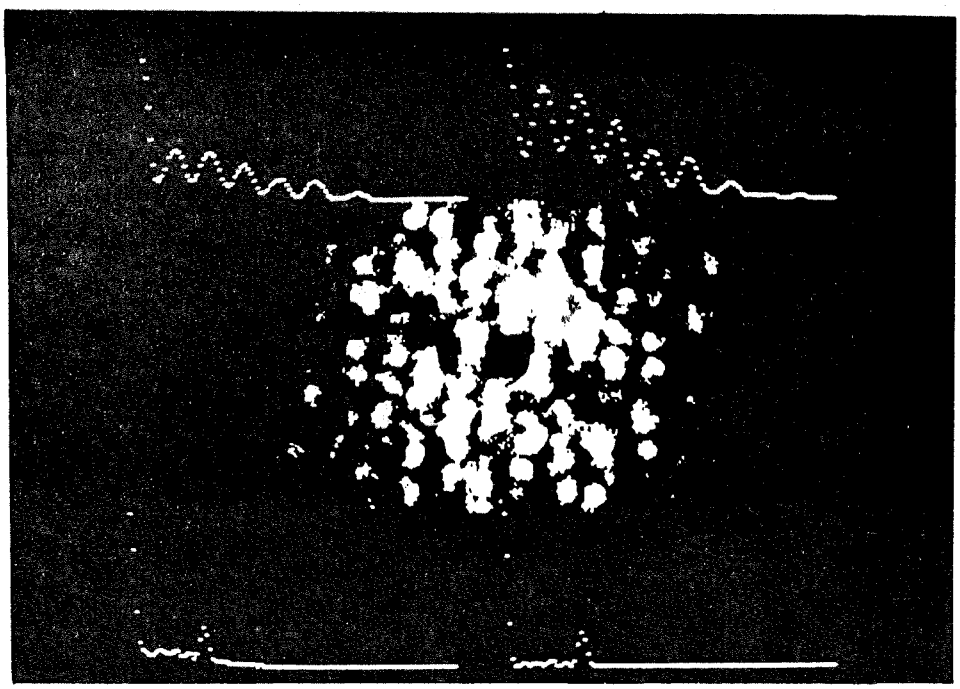


FIG 11

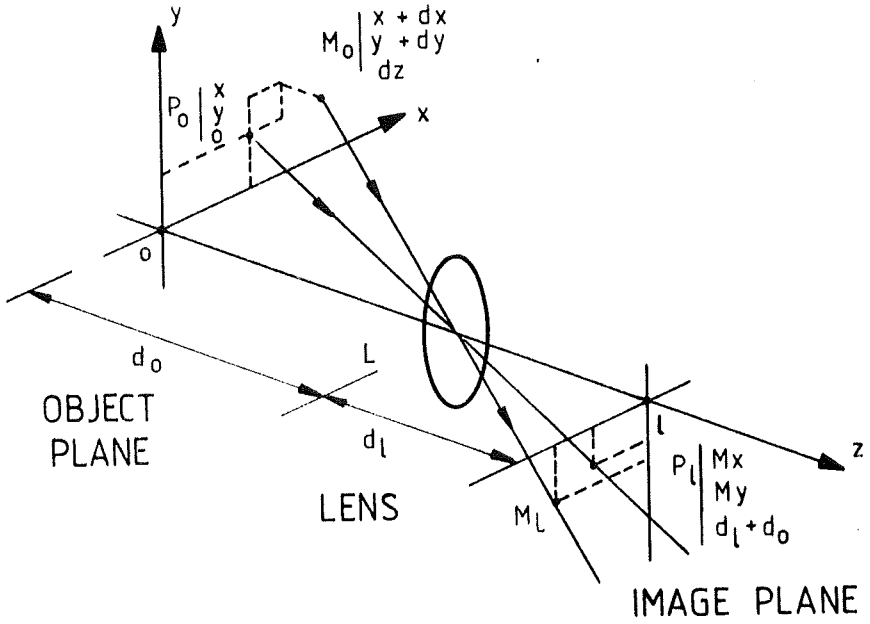


FIG. 12 - IMAGING SYSTEM

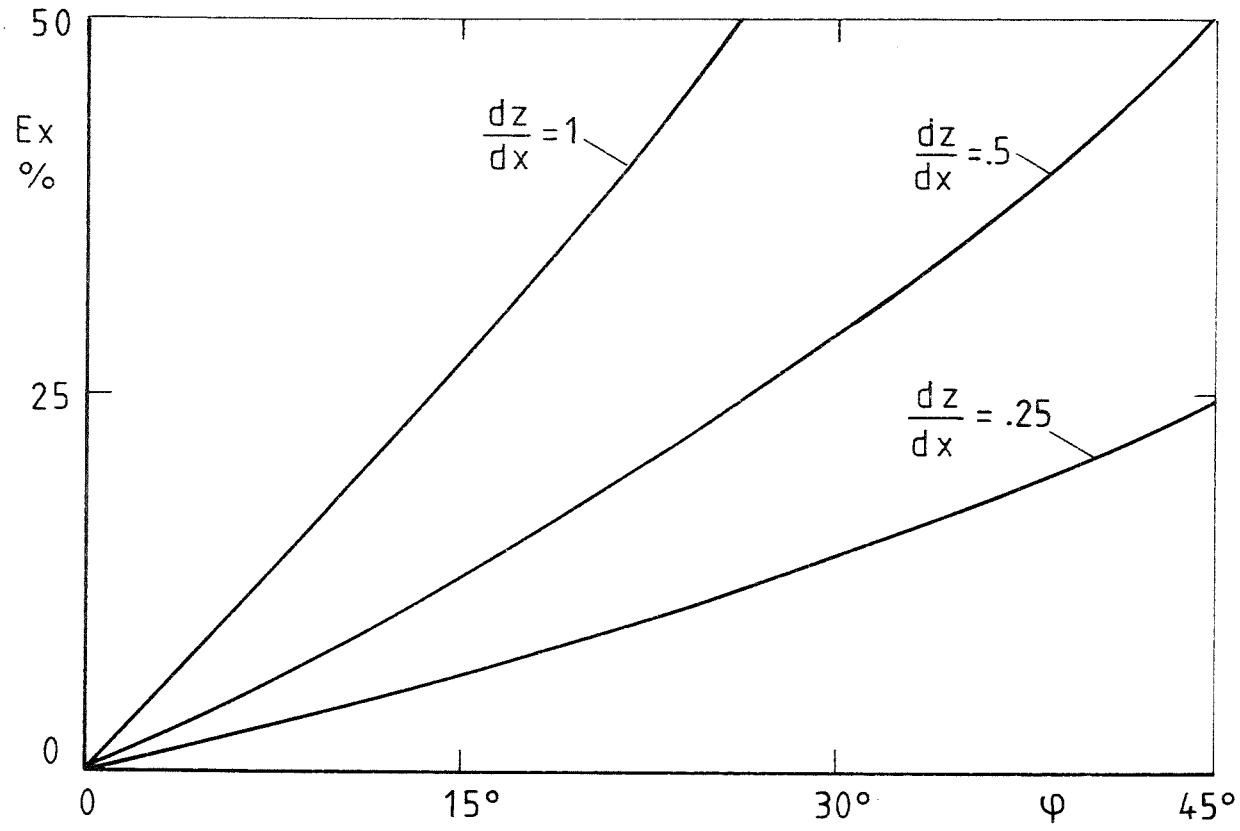


FIG.13 - THEORETICAL RELATIVE ERROR OF IN PLANE COMPONENT DUE TO OUT-OF-PLANE MOTION

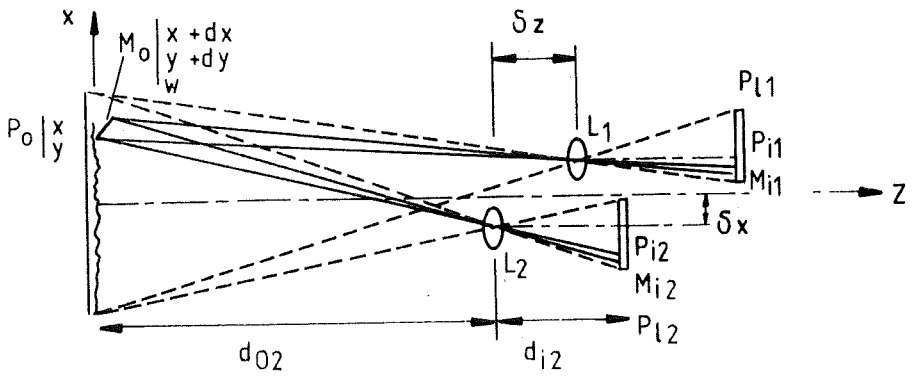


FIG. 14 - SIMULTANEOUS RECORDING OF TWO DOUBLE EXPOSURE PHOTOGRAPHIC PLATES TO MEASURE THE THREE COMPONENTS OF DISPLACEMENT

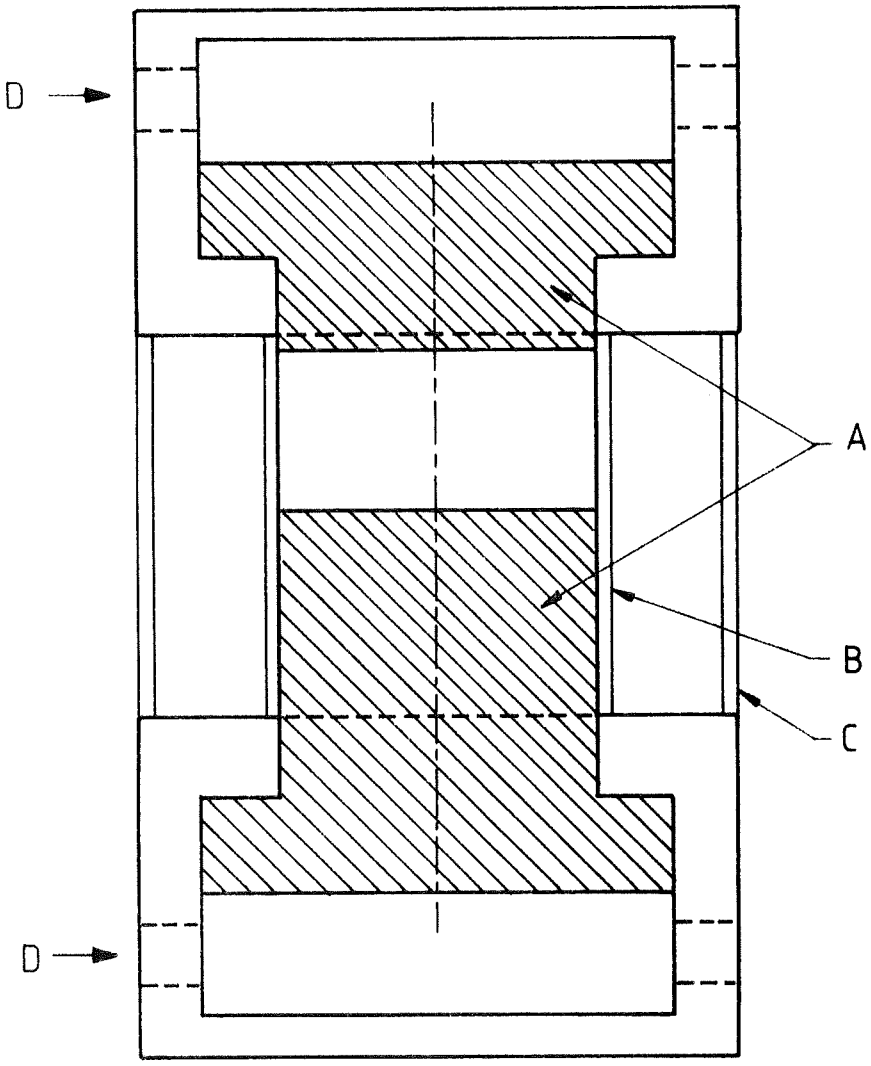


FIG. 15

CONVECTION CELL

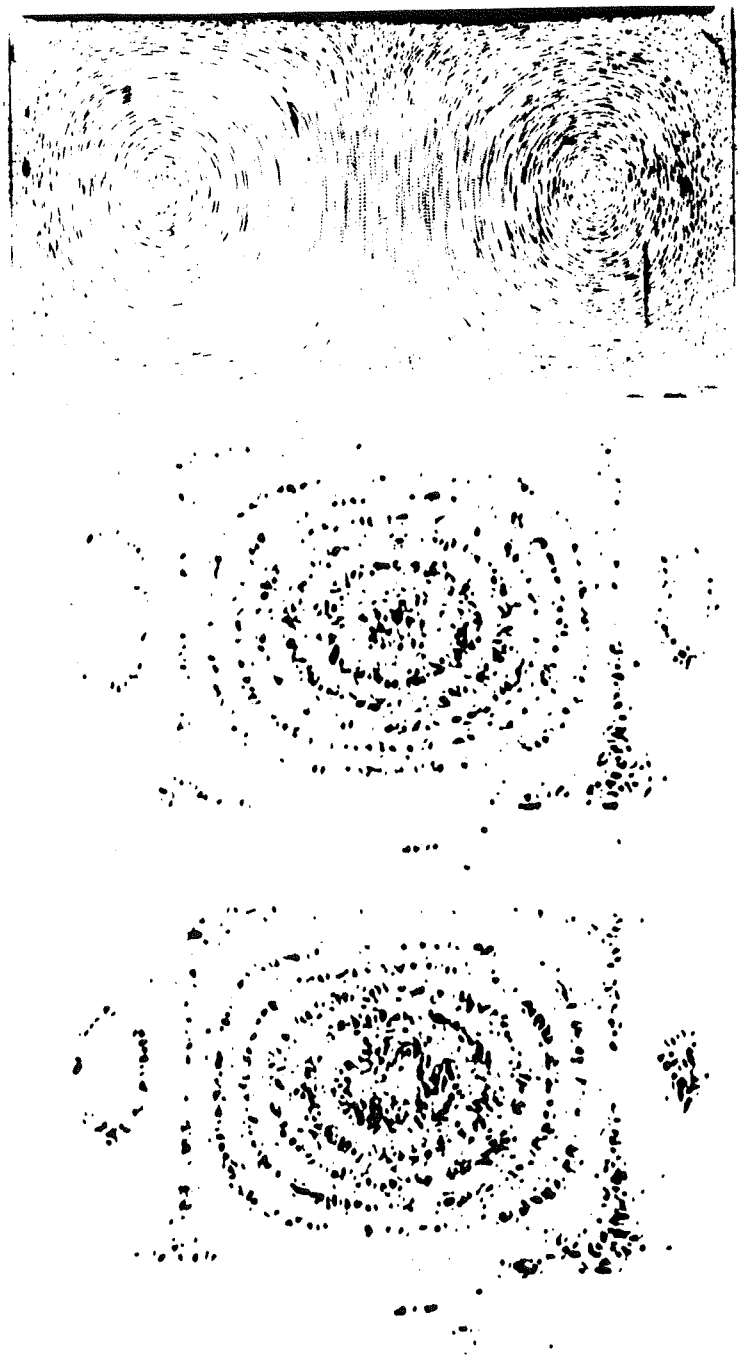


FIG 16

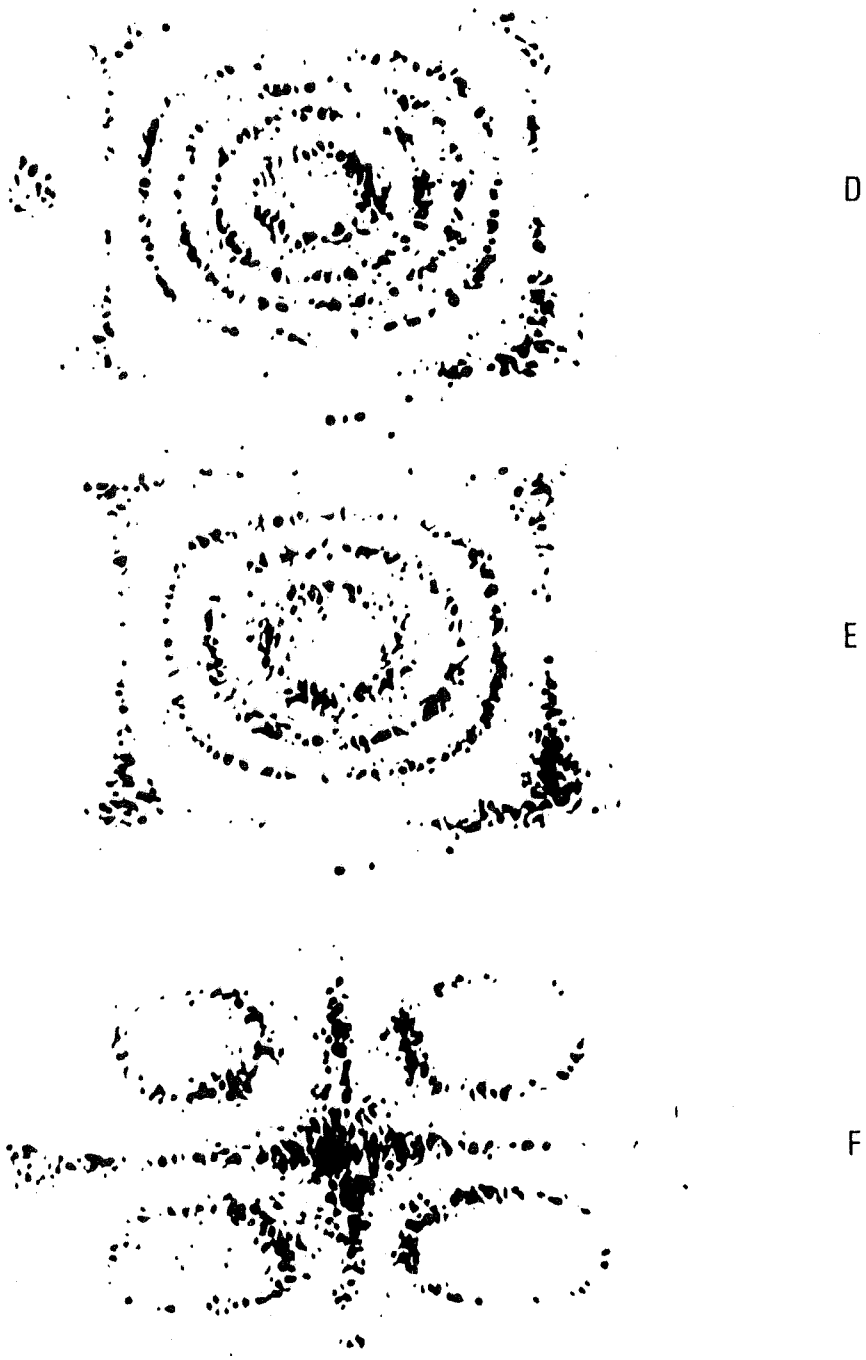


FIG 16

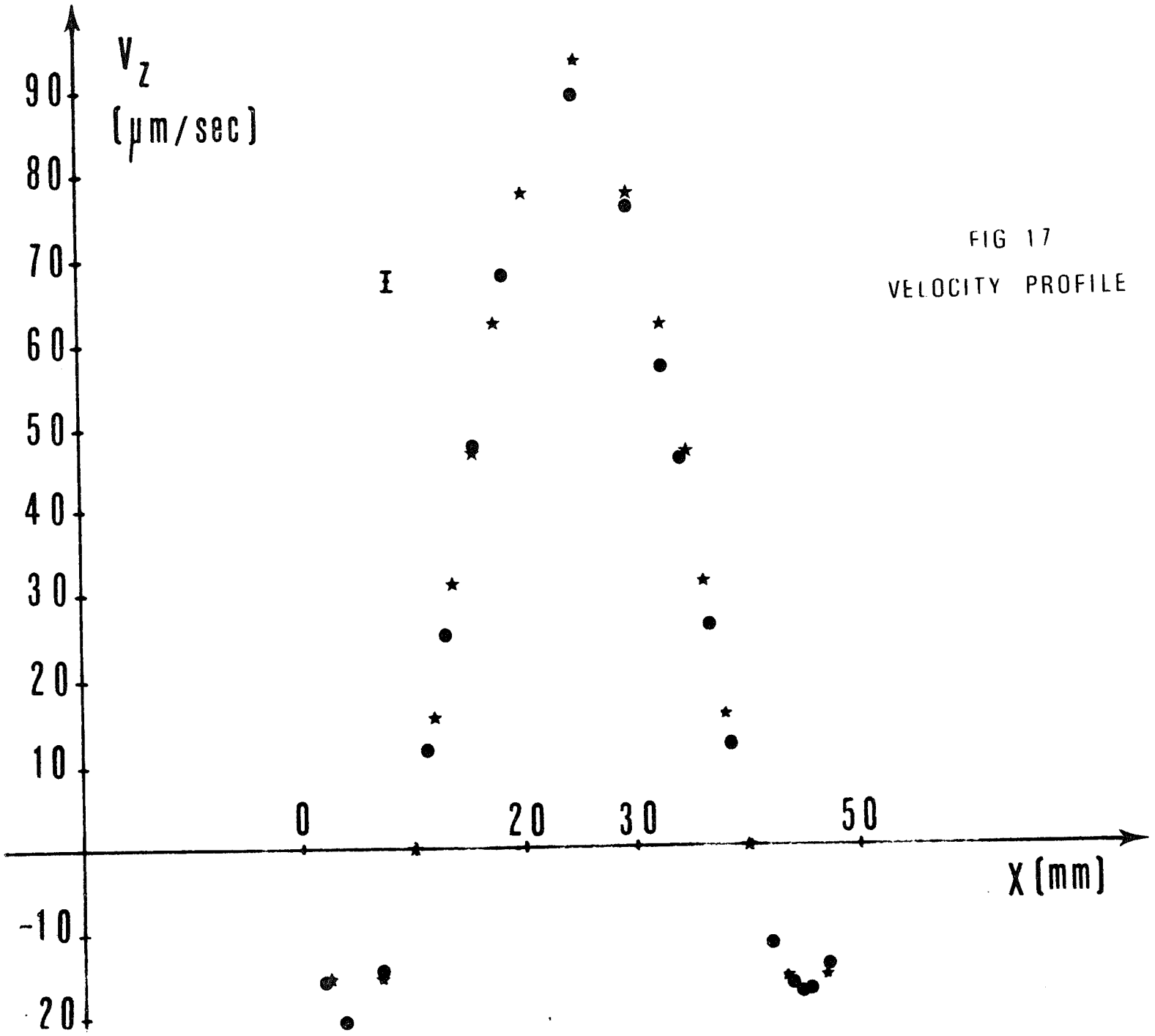


FIG 17

VELOCITY PROFILE

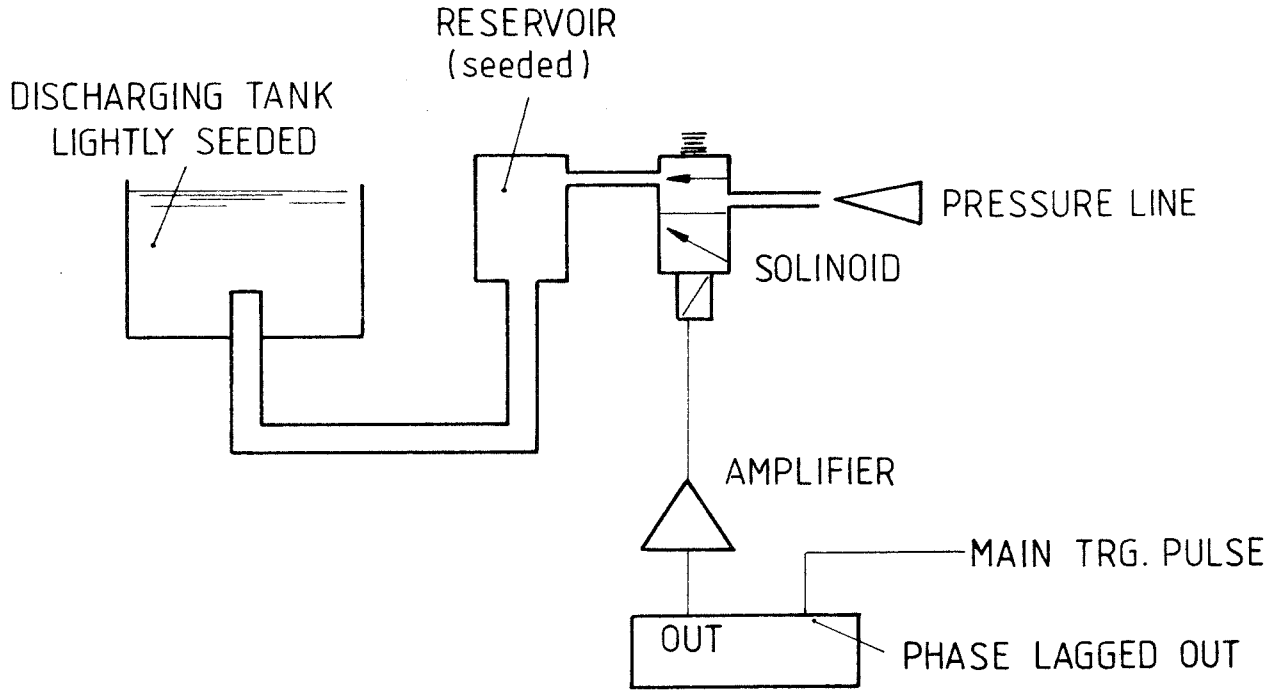


FIG. 18 - TESTING ARRANGEMENT.

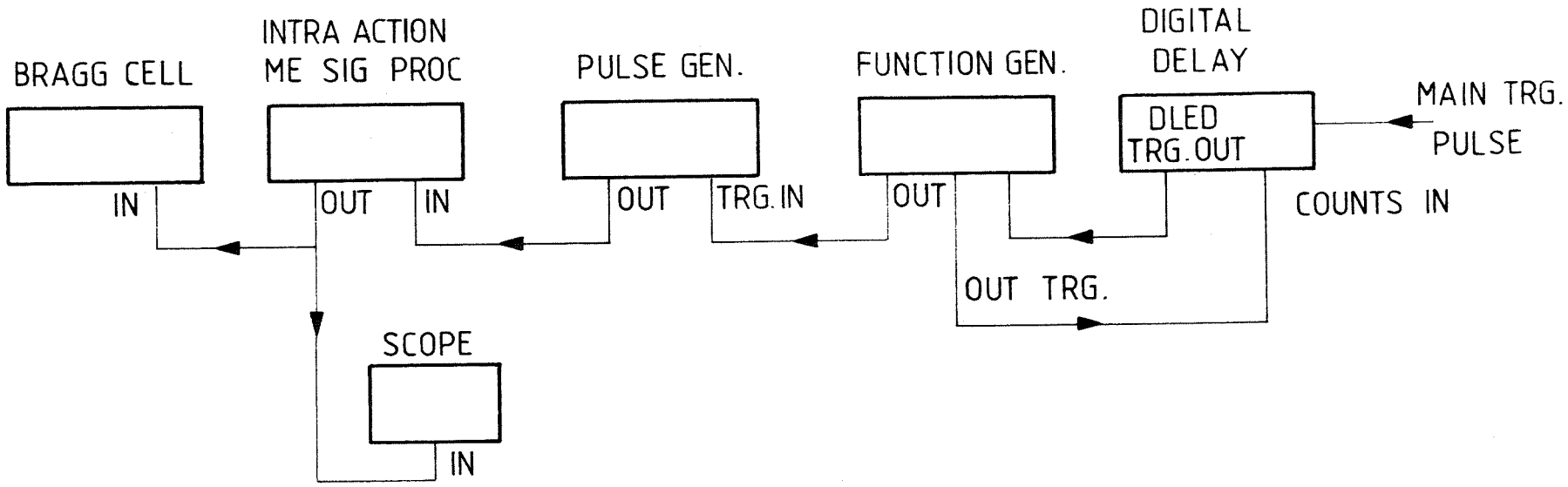


FIG. 19 - SKETCH OF BRAGG CELL SHUTTER

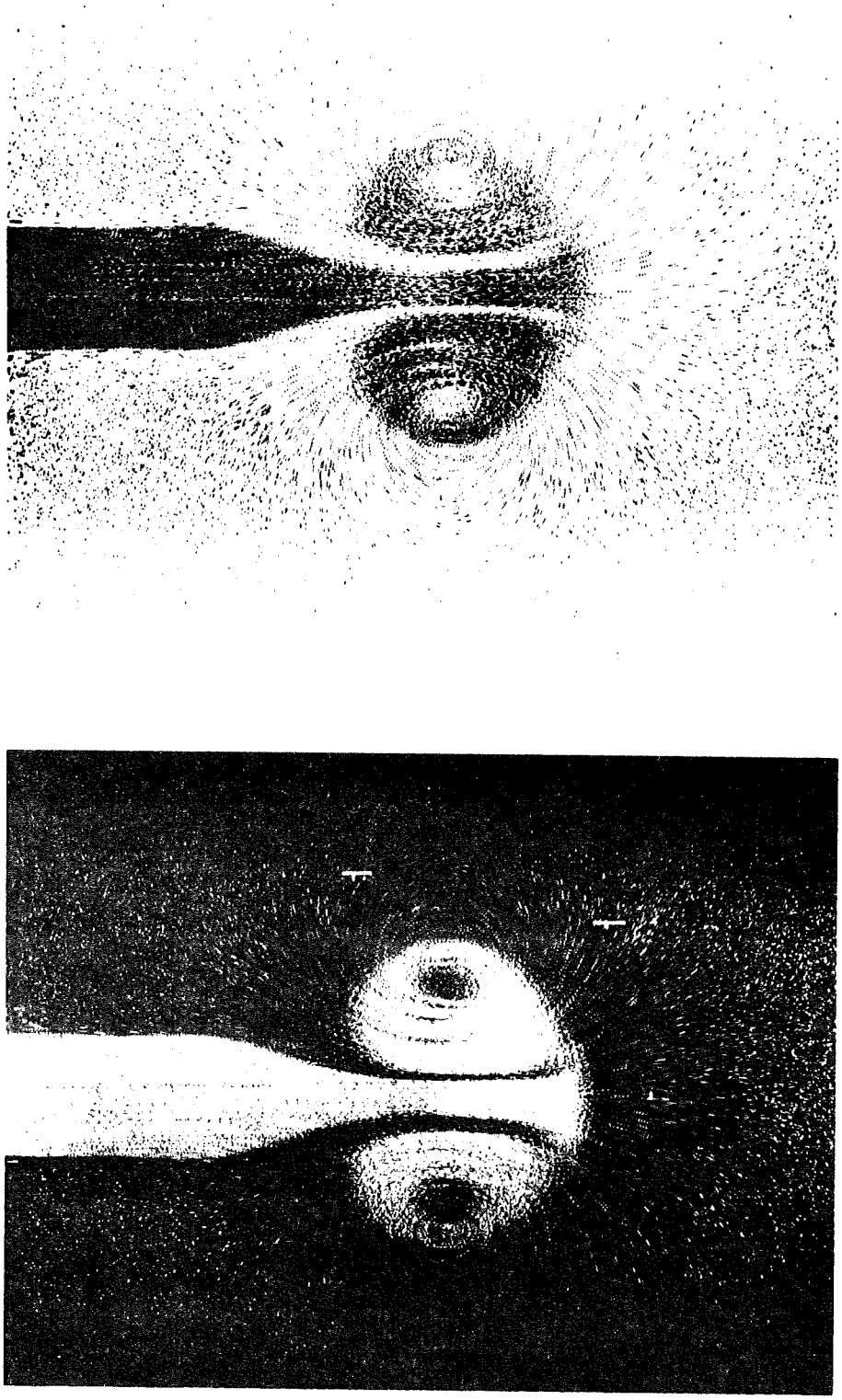


FIG 20

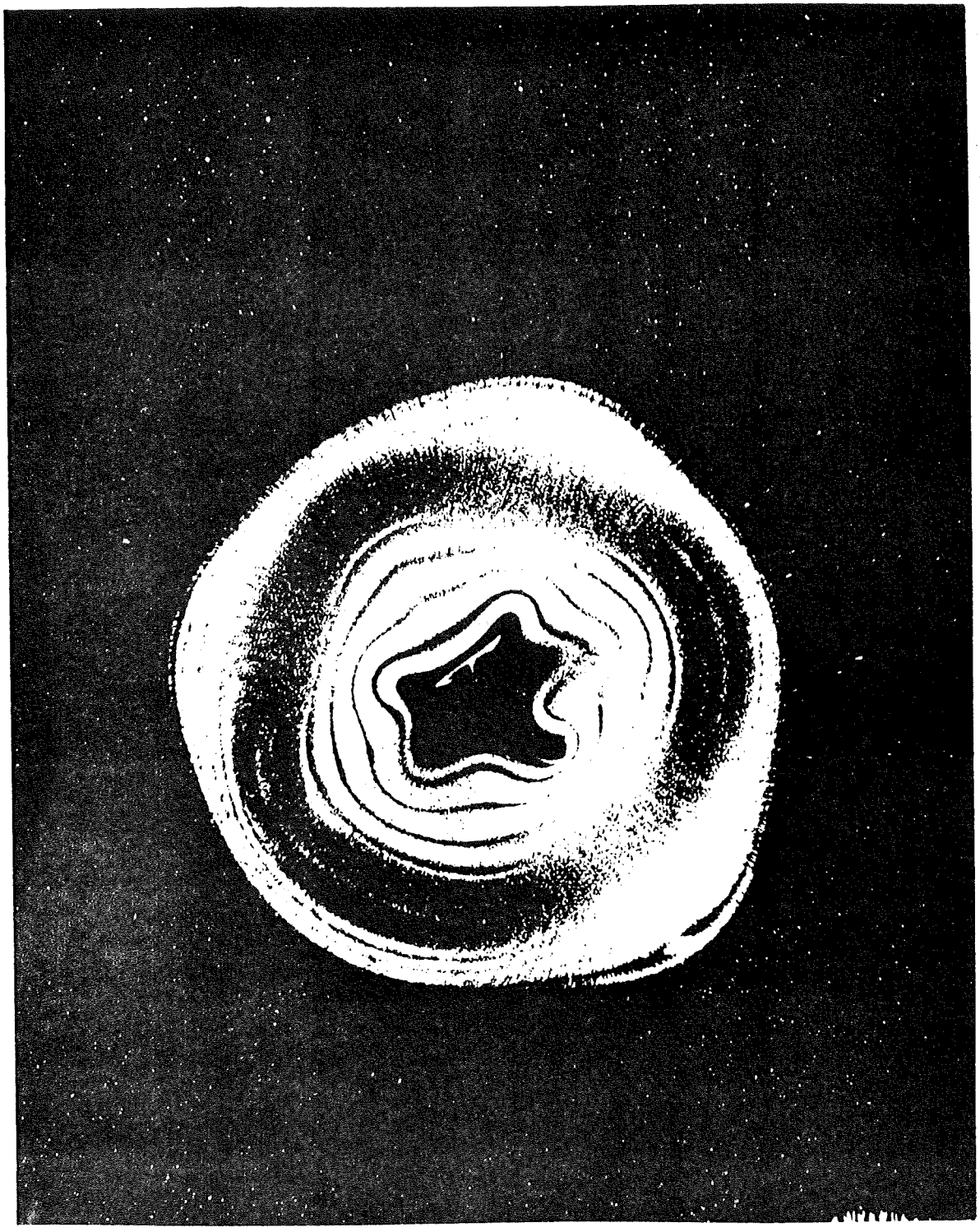


FIG 21 A



FIG 21 B

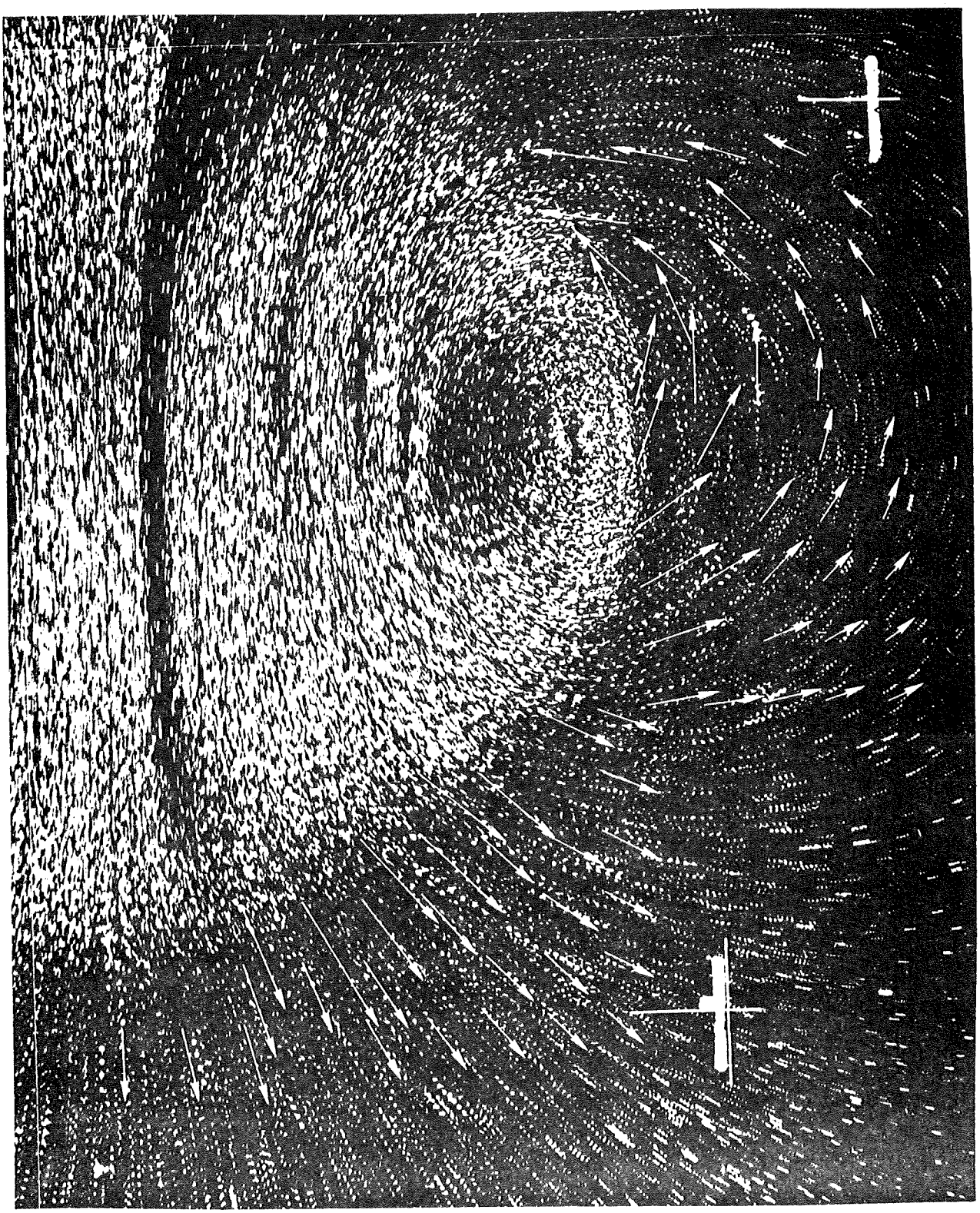


FIG 22
VELOCITY MAP

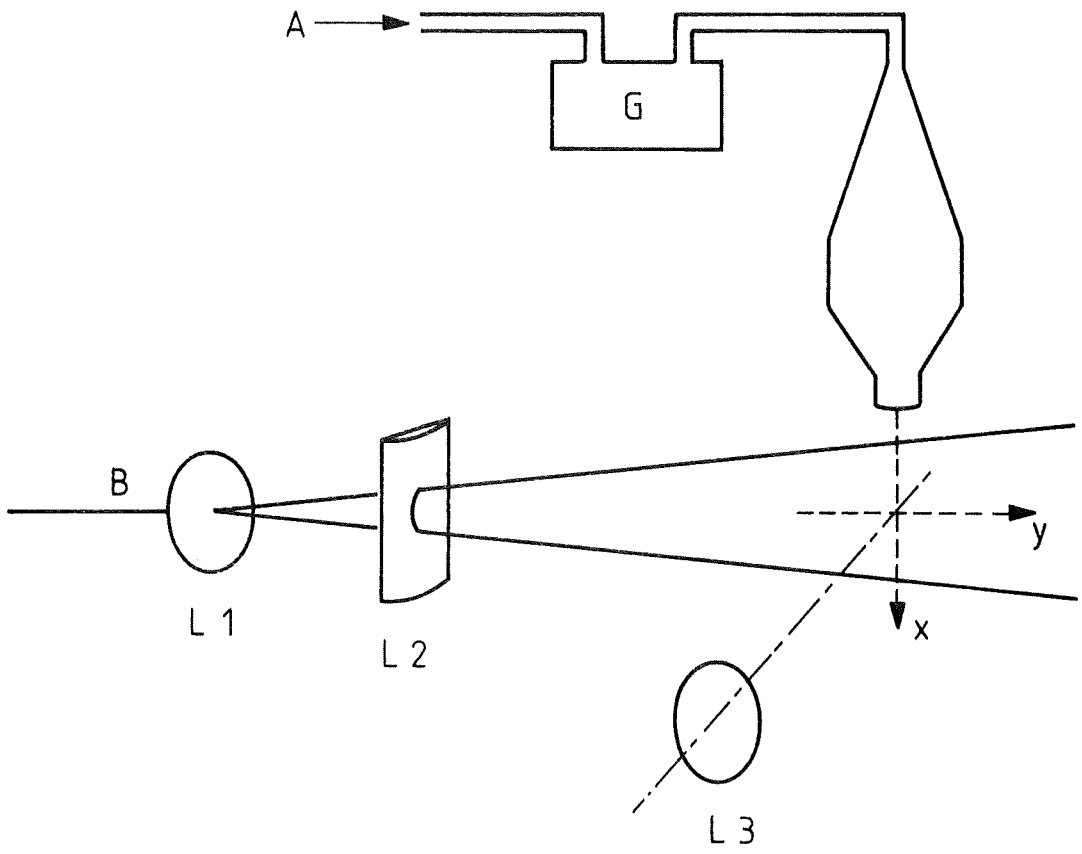


FIG. 23

EXPERIMENTAL SETUP

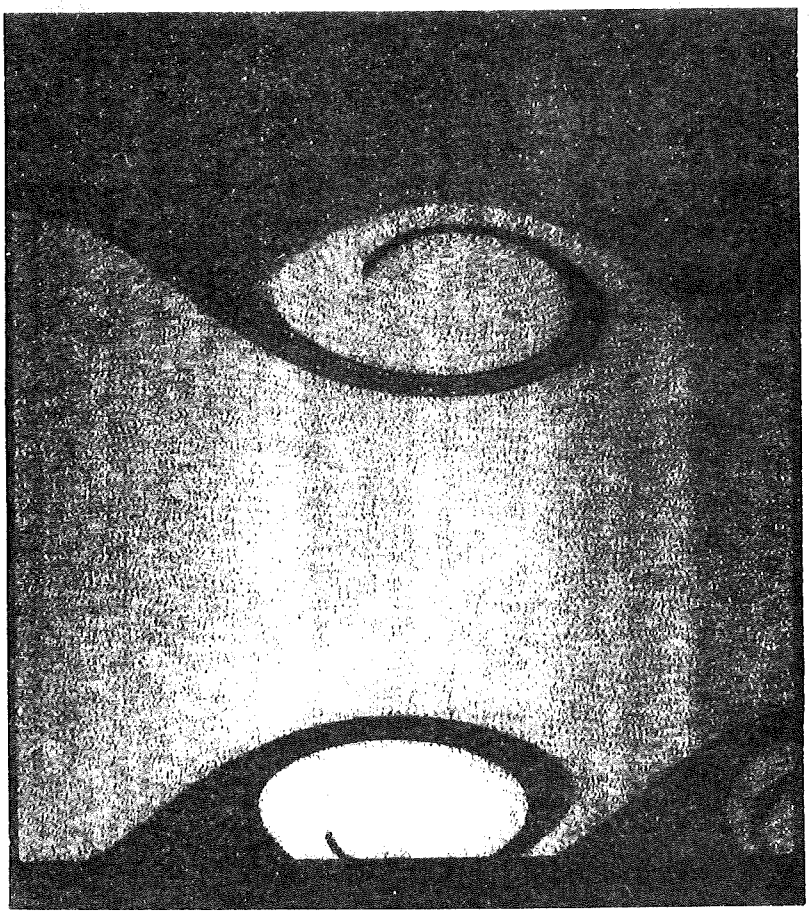


FIG 24

VORTEX

RING

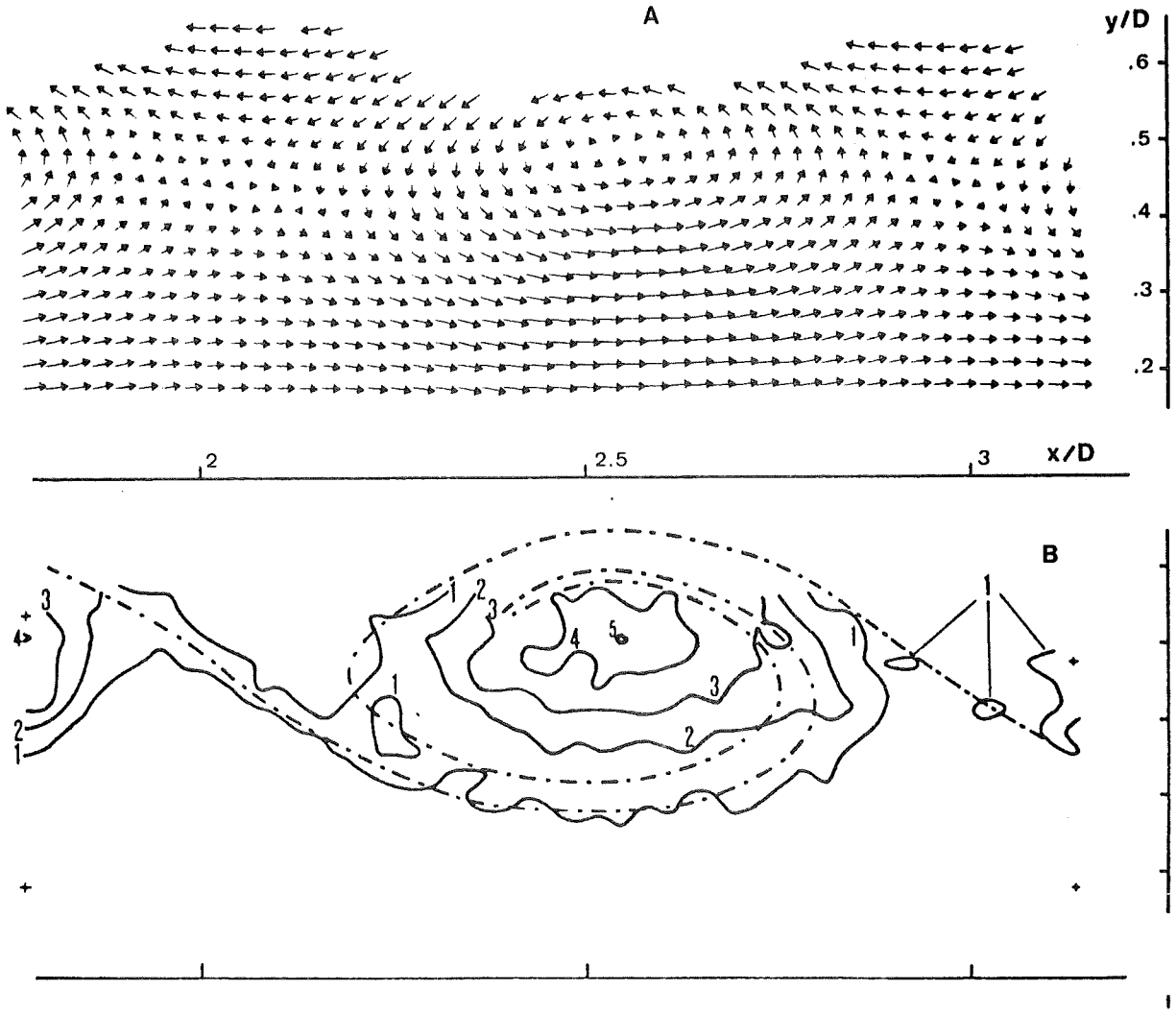


FIG 25

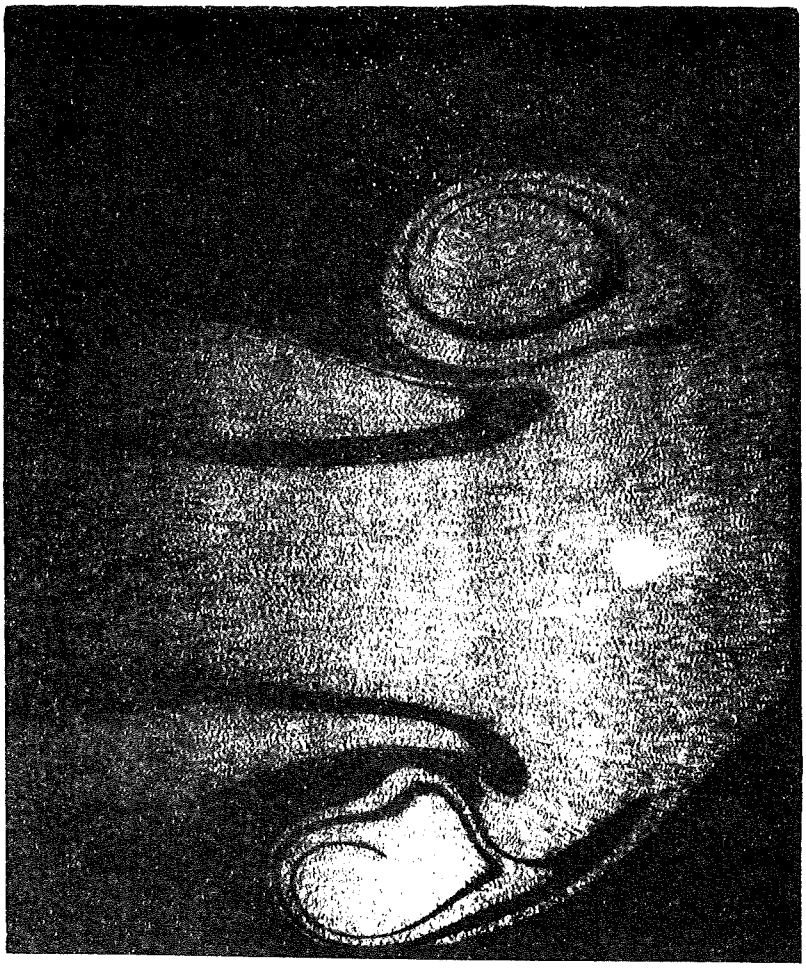


FIG 26

PAIRING EVENT

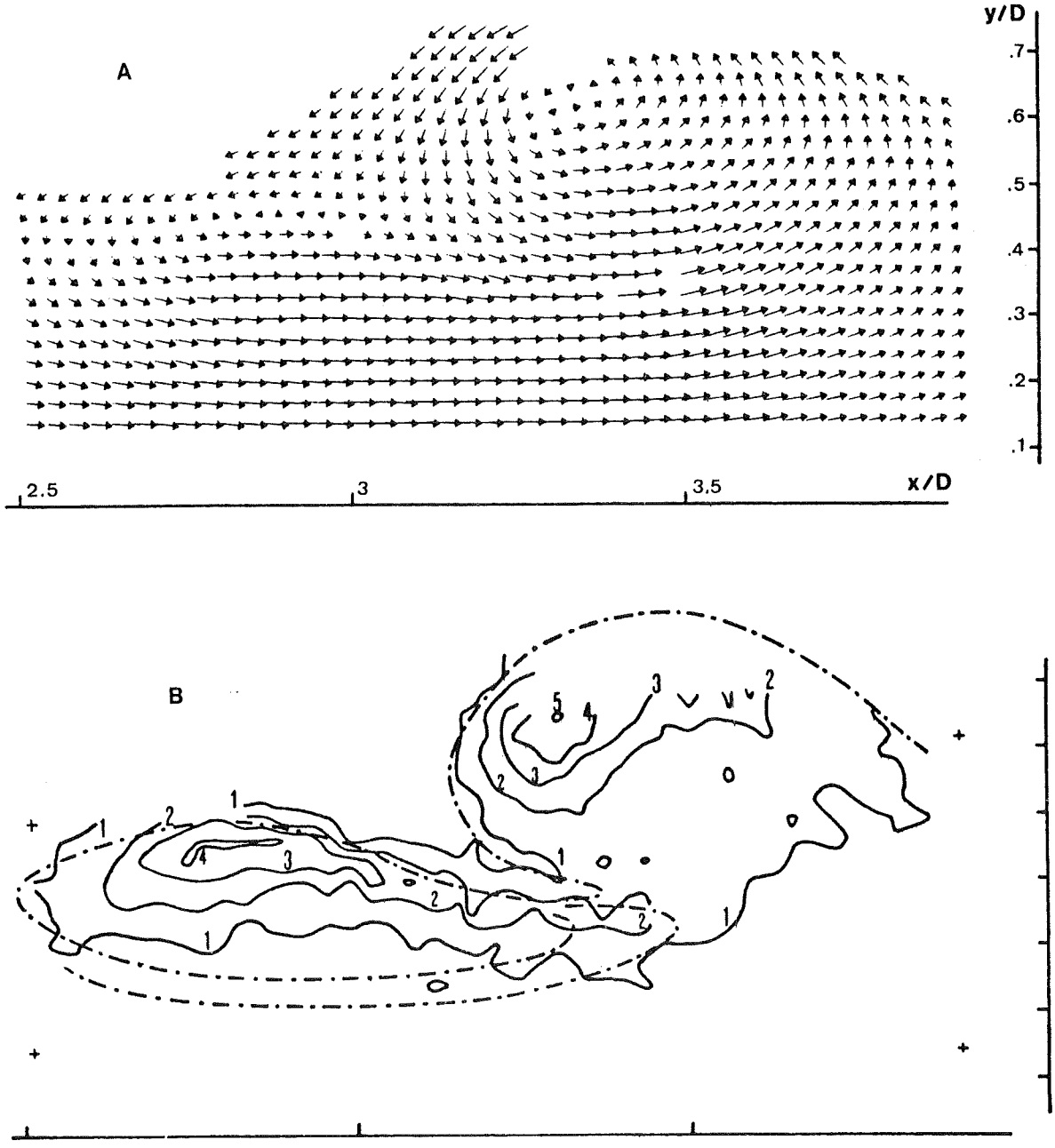


FIG 27



FIG 28

LARGE SCALE STRUCTURE

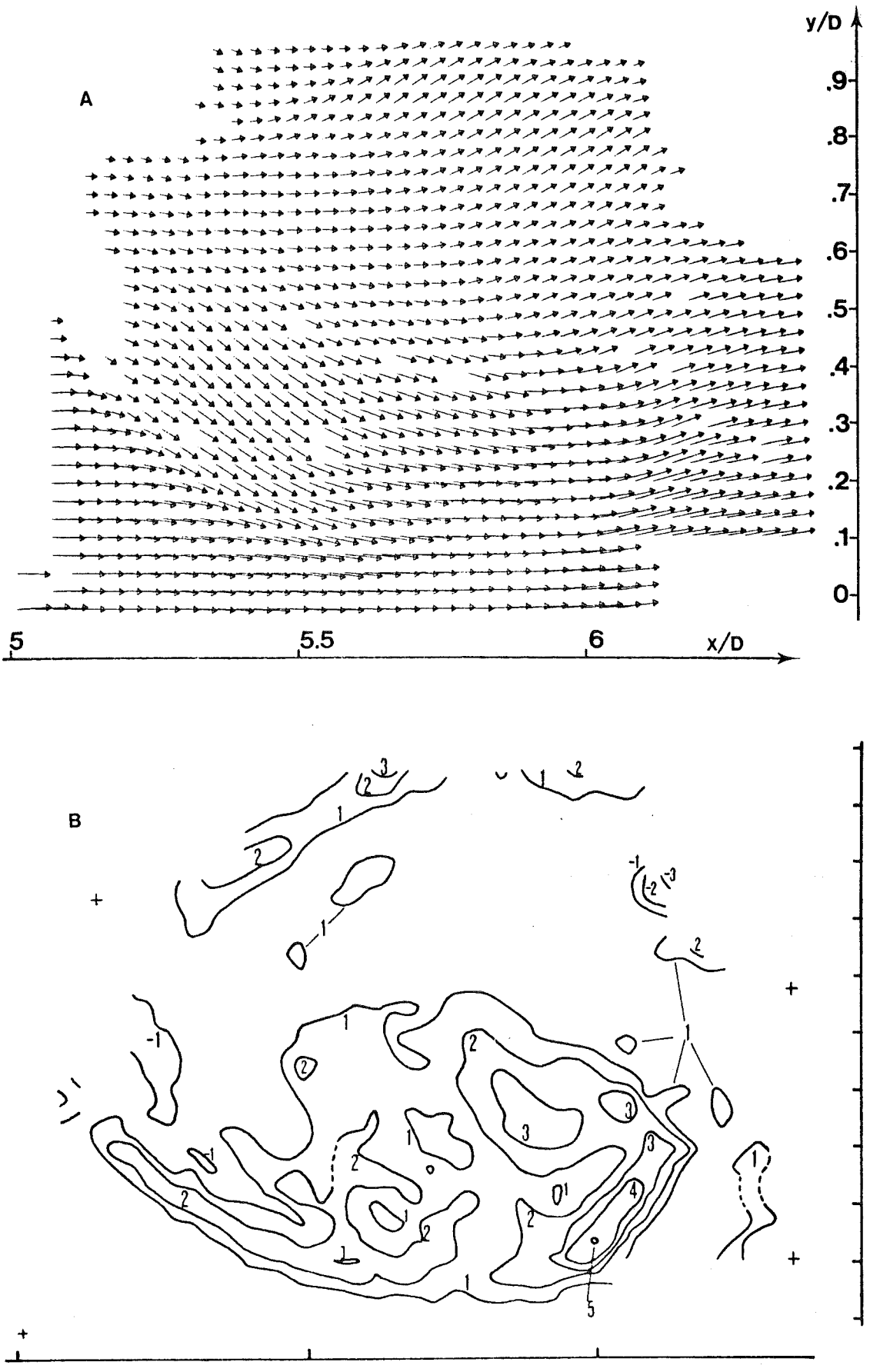


FIG 29